Title
DOUBLE-CHARGE-EXCHANGE AND INELASTIC SCATTERING IN x- + 3He

Permalink
https://escholarship.org/uc/item/7vj7n7b5

Author
Sperinde, Johnie M.

Publication Date
1971-08-01

DOUBLE-CHARGE-EXCHANGE AND INELASTIC SCATTERING IN $\pi^- + {}^3He$

Johnie M. Sperinde
(Ph. D. Thesis)

August 4, 1971

Prepared for the U.S. Atomic Energy Commission under Contract W-7405-ENG-48

DISCLAIMER

DOUBLE-CHARGE-EXCHANGE AND INELASTIC SCATTERING IN $\pi^- + {}^3He$

Contents

DOUBLE-CHARGE-EXCHANGE AND INELASTIC SCATTERING IN $\pi^- + {}^3He$

Johnie M. Sperinde

Lawrence Berkeley Laboratory
University of California
Berkeley, California

August 4, 1971

ABSTRACT

The reactions $\pi^- + {}^3He \rightarrow \pi^+ + 3n$ and $\pi^- + {}^3He \rightarrow \pi^- + {}^3He^*$ were studied to investigate the T = 3/2 three nucleon system. The differential cross sections were measured at 140 MeV incident pion energy for a scattering angle of about 30 deg. The secondary pion was momentum analyzed in a magnetostrictive-readout wire-chamber spectrometer. The double-charge-exchange reaction yielded a secondary pion energy distribution which can be explained either as a T = 3/2 three-nucleon resonance or as a consequence of the low relative momenta of the nucleons in the ${}^3He$ nucleus. No evidence of the effects observed in the double-charge-exchange reaction was seen in the inelastic scattering reaction. This was probably due to the proximity to the bound state of ${}^3He$.

I. INTRODUCTION

A. Three Neutrons

The three-nucleon system has received considerable attention in recent years. The two-nucleon system is now well understood. The basic question is whether our knowledge of the two-nucleon system is sufficient to understand the behavior of the three-nucleon system or if additional three-body forces are present. To investigate this question one needs to compare the results of calculations assuming only two-body forces with the experimentally observed three-nucleon system.

The simplest of the three-nucleon systems consists of three neutrons. There are no coulomb forces, the particles are identical, and the isospin state is pure $T = \frac{3}{2}$. This system has been theoretically studied by a number of authors.[1-4] Mitra and Bhasin concluded that the ^3P nucleon-nucleon interaction dominates in the three neutron system. Using separable potentials compatible with the two-nucleon data they estimated that it is possible for the three neutron system to be bound. They gave as the most likely quantum numbers (LSJ) = $(1\ \frac{3}{2}\ \frac{1}{2})$, with $(1\ \frac{3}{2}\ \frac{3}{2})$ somewhat less likely. Note that spin-isospin independence of nuclear forces implies that a $T = \frac{3}{2}$, $S = \frac{1}{2}$ trineutron bound state would be reflected in the $T = \frac{1}{2}$, $S = \frac{3}{2}$ three nucleon system.[5] An $S = \frac{1}{2}$ trineutron would be in contradiction to the $T = \frac{1}{2}$ scattering data. Okamoto and

Davies, using variational techniques and the potential of Pease and Fesbach,[6] also concluded $(1\ \frac{3}{2}\ \frac{1}{2})$ is the most likely state but concluded that three neutrons are unbound by approximately 10 MeV. Benöhr,[7] assuming the two-nucleon potentials of Afnen and Tang[8] or Eikemeier and Hockenbroich,[9] concluded that there is a resonance about 1 MeV above threshold. He gave the quantum numbers $(1\ \frac{1}{2}\ -)$ for the resonance. This state corresponds to a P-wave neutron moving in the tail of the virtual deuteron.

Searches for bound states of three neutrons have been carried out by several groups of experimenters.[10-12,15] With the possible exception of the experiment by Adjacic et al., no evidence of a bound state of three neutrons has been seen. Similar searches have been made for the corresponding bound state of three protons with the same negative results.[13,14] At the present time the non-existence of a bound state of three neutrons seems well established. Subsequent work on the $T = \frac{3}{2}$ three nucleon system has been concentrated on looking for resonances in the continuum spectra of several different reactions.[15-19] In all the reactions studied distributions which differ from phase space distributions have been obtained. These deviations have been interpreted in various ways by the different groups of experimenters. Tombrello and Slobodrian conclude that the triton spectrum obtained from the reaction $^3He(^3He, t)3p$ at 50 MeV is distorted by the Coulomb interaction of the triton and the three protons. Kaufman et al. suggest that the proton spectrum obtained from the reaction $^{4}He(\pi^-, p)3n$ at 140 MeV may indicate a three-neutron resonance. Ohlsen et al. report that their data from the reaction $^{3}H(t, {}^{3}He)3n$ at 22 MeV suggest the existence of a virtual state in the three neutron system in the range 1.0 to 1.5 MeV above the three-neutron mass. Bacher et al. explain the departure of their energy spectrum from phase space in the reaction $^{3}He(p, n)3p$ at 25MeV as a $^{1}S_{o}$ final-state interaction between two protons. Williams et al. studied the same reaction at 50 MeV and interpreted their results as indicating a three proton resonance at 16 ± 1 MeV excitation energy relative to the ground state of ^{3}He. It is apparent from the diversity of the above interpretations that a model is needed which can simultaneously explain the results of the above experiments. Additional experimental data will also be needed to check against the predictions of such a model.

An alternative method of producing three neutrons in the final state is the double-charge-exchange (DCX) reaction $\pi^- + {}^{3}He \rightarrow \pi^+ + 3n$. For reasons discussed in the next section it was expected that the results of this reaction could be easily interpreted. Any effect observed in the three-neutron system should also be evident in the system of two-protons and a neutron. For this reason both double-charge-exchange and inelastic scattering of negative pions on ^{3}He were studied.

B. Double-Charge-Exchange

The double-charge-exchange of pions on nuclei, originally suggested by Drell and de Shalit, produces final states with large excesses of protons or neutrons. The reaction is generally assumed to occur as a cascade of successive charge exchanges on individual nucleons in the nucleus.[20-24] This model correctly accounted for the cross section variations as a function of the total energy and the energy distribution of secondary mesons.[23] However, as pointed out by Becker and Schmit,[25] the calculated angular distributions are peaked in the forward direction, whereas the measured angular distributions are almost isotropic. They interpret this discrepancy as indicative of the double-charge-exchange taking place preferentially on a pair of nucleons, rather than as a cascade process on individual nucleons.

A general feature of the double-charge-exchange reactions which have been studied is the small deviation of the secondary pion from the energy distribution predicted by the statistical model.[15,23,24,26] Thus significant deviations from the predictions of the statistical model may be interpreted as the result of final state interactions.

II. EXPERIMENTAL METHOD AND APPARATUS

A. General Method

This experiment was designed to observe reactions of the type $\pi^- + {}^3He \rightarrow \pi^\pm + X$, with the invariant mass distribution of X the main quantity of interest. The invariant mass of X can be determined by measuring the scattered pion momentum and direction for a fixed energy pion beam incident on a target of ^3He. Reactions leading to charged particles in the final state include the following (assuming no pion production):

$$
\begin{array}{lll}
\pi^- + {}^3He \rightarrow & \pi^- + {}^3He & \text{-- elastic scattering} \\
& \pi^- + {}^3He^* & \\
& \pi^- + p + d & \text{-- inelastic scattering} \\
& \pi^- + 2p + n & \\
& \pi^0 + (pnn) & \\
& \hookrightarrow \gamma\gamma & \\
& \quad \hookrightarrow e^+e^- & \text{--charge exchange} \\
& \pi^0 + (pnn) & \\
& \hookrightarrow \gamma e^+e^- & \\
& \pi^+ + 3n & \text{--double-charge-exchange}
\end{array}
$$

Thus it was necessary to be able to discriminate between π^+, p, d, t, ^3He and e^+.

A diagram of the experimental setup is shown in figure 1. A beam of π^- of energy 140 MeV (momentum 242 MeV/c) was incident on a target of ^3He. The energy of the beam was selected to be near the

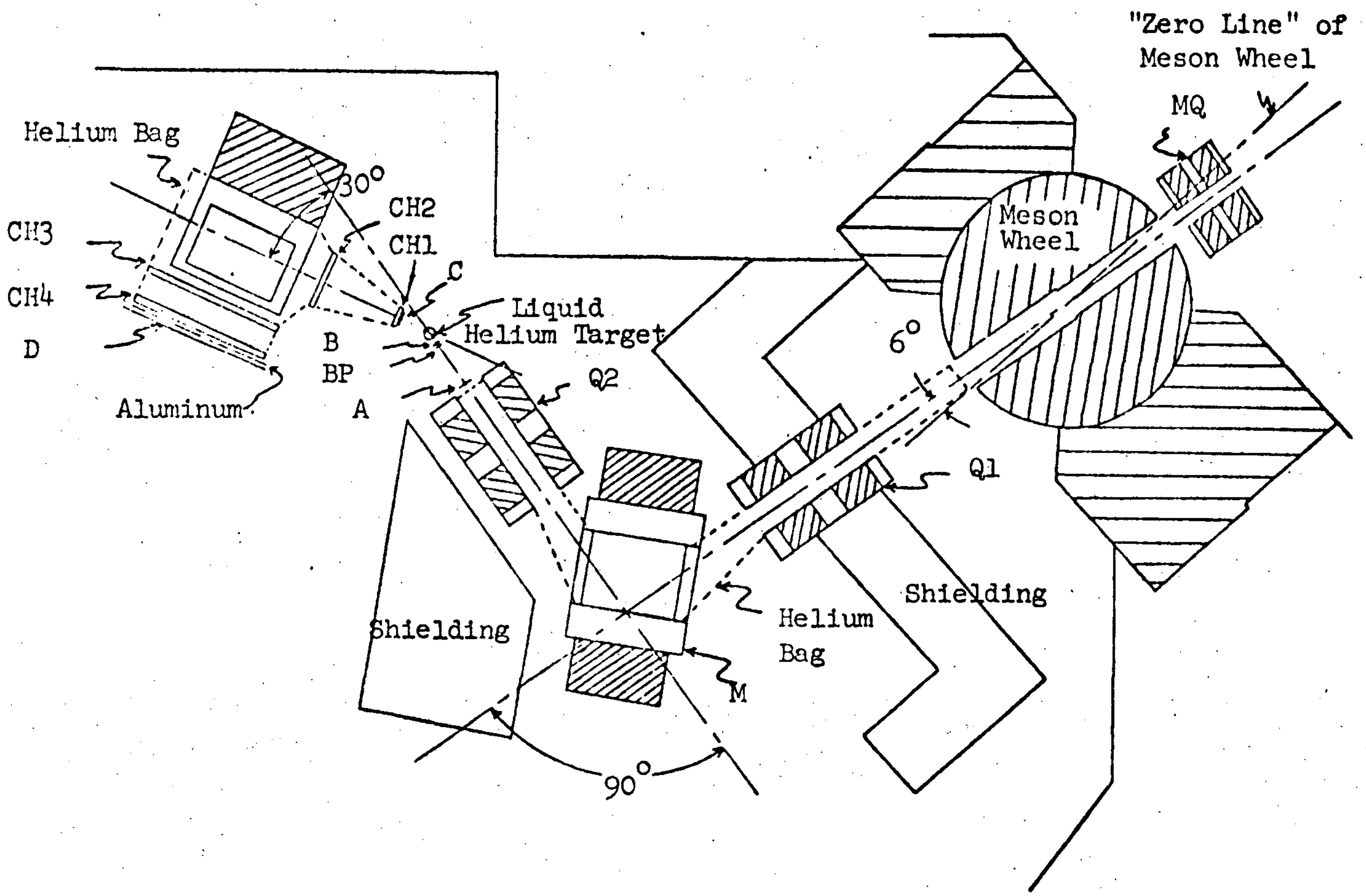

Figure 1. Experimental set-up; MQ, Q1, and Q2 are doublet quadrupole magnets; M is a bending magnet; A,B,BP,C and D are counters, and CH1-CH4 are spark chambers.

$\Delta(1236)$ pion-nucleon resonance so that the DCX cross section would be relatively large and below the pion-production energy-threshold in order to minimize the background reactions. The direction of the incoming π^- was determined with two scintillation counter hodoscopes (A and B). The momentum and direction of the outgoing $\pi^{\pm}$ were observed with a wire-chamber spectrometer consisting of four wire chambers, two on each side of an analyzing magnet. The central axis of the spectrometer was at an angle of 30 degrees with respect to the central beam line and allowed the detection of events over a range of scattering angles from 15 to 45 degrees. The DCX cross section was expected to be peaked in the forward direction. The final positioning of the spectrometer was a compromise between the small angle desired from cross section considerations and a large enough angle so that the upstream spark chambers in the spectrometer would not be swamped with beam particles. The solid angle acceptance of the spectrometer was approximately 22.5 msr at 170 MeV/c and decreased linearly to 9 msr at 100 MeV/c and 17 msr at 250 MeV/c (see figure 2 and appendix C). A 0.5 inch thick sheet of aluminum following the last spark chamber stopped the heavy charged particles in the momentum range of interest and prevented them from triggering the system.

The triggering logic consisted of a signal from each of the beam hodoscopes (A and B) and an additional beam counter BP, and signals from a counter C in front of the first spark chamber and a set of counters D behind the fourth spark chamber and aluminum

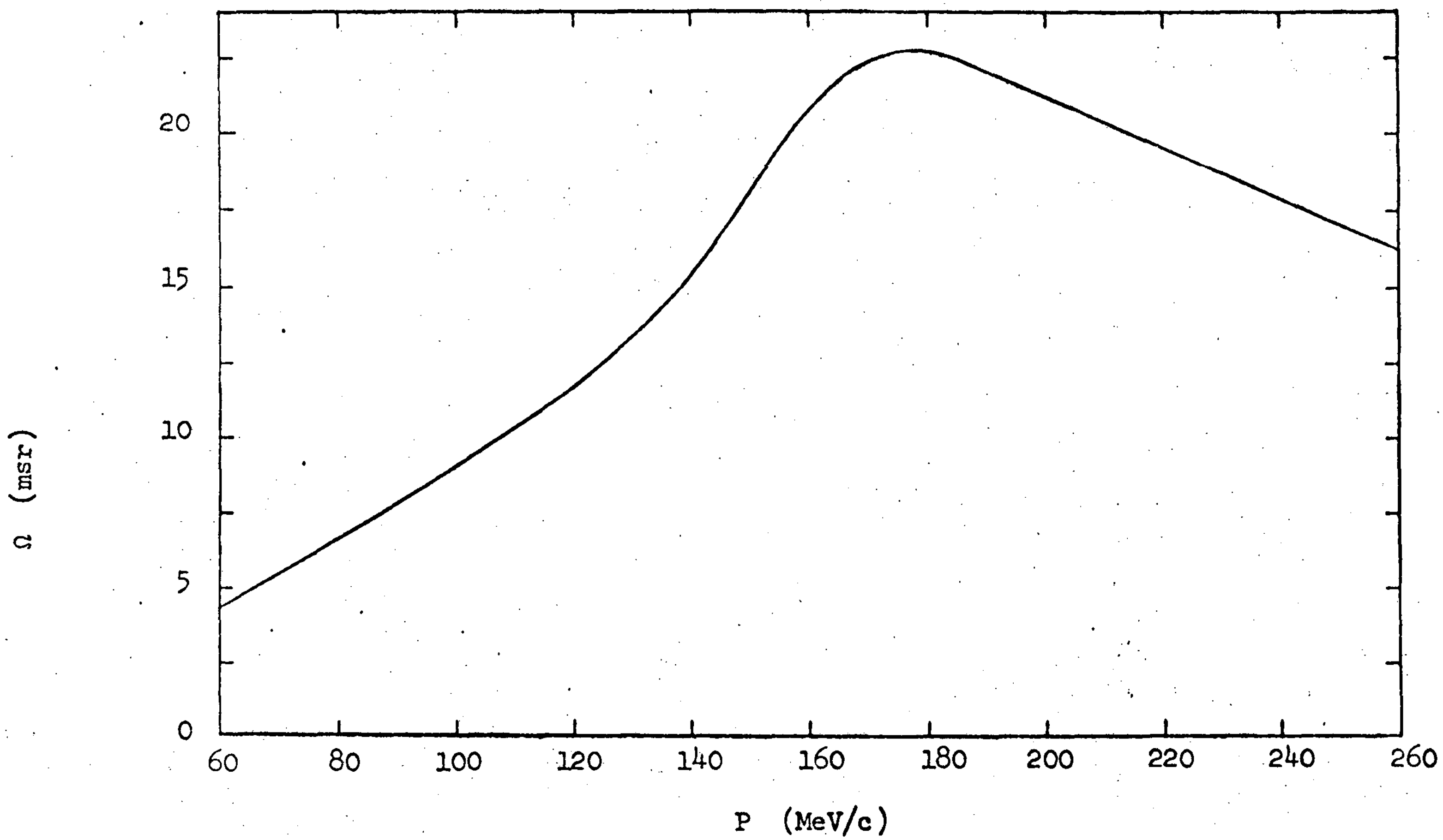

Figure 2. Spectrometer solid angle acceptance as a function of momentum.

absorber. The change in the sign of the recorded pion from + to - was accomplished by reversing the direction of the magnetic field in the spectrometer analyzing magnet.

B. Beam

The beam design, as shown in figure 3, was governed by the requirements of high flux needed to study the low cross section double-charge-exchange reaction and of good energy resolution desired for inelastic scattering. These requirements were satisfied with basically the same beam setup. A dispersed beam, in which position at the target is a function of momentum, was used for achieving good energy resolution and a momentum-focused beam was used for achieving the high flux. This was done in the following way: The dispersed beam was produced by bending the pions through two nearly equal large angle bends, one in the cyclotron fringe field and the other in an external bending magnet. The momentum-focused beam was obtained by focusing the beam midway between the two bends, which in effect reverses the direction of the second bend and thus gives a momentum focus. More details of the beam design are given below.

The 735 MeV internal proton beam of the 184-inch cyclotron was incident on a $\frac{1}{2}$ x 1 x 3 inch beryllium target. Negative pions of an energy of 140 MeV produced in the forward direction were bent approximately 110 degrees in the cyclotron fringe field. The pions then passed through the internal meson quadrupole (MQ) which was adjusted to give a parallel beam (see solid curves in figure 3). The beam was deflected 90 degrees by the bending magnet M and then focused at the ^{3}He target by the quadrupole magnet Q2. The momentum-focused beam was obtained by adjusting MQ to produce a horizontal focus midway

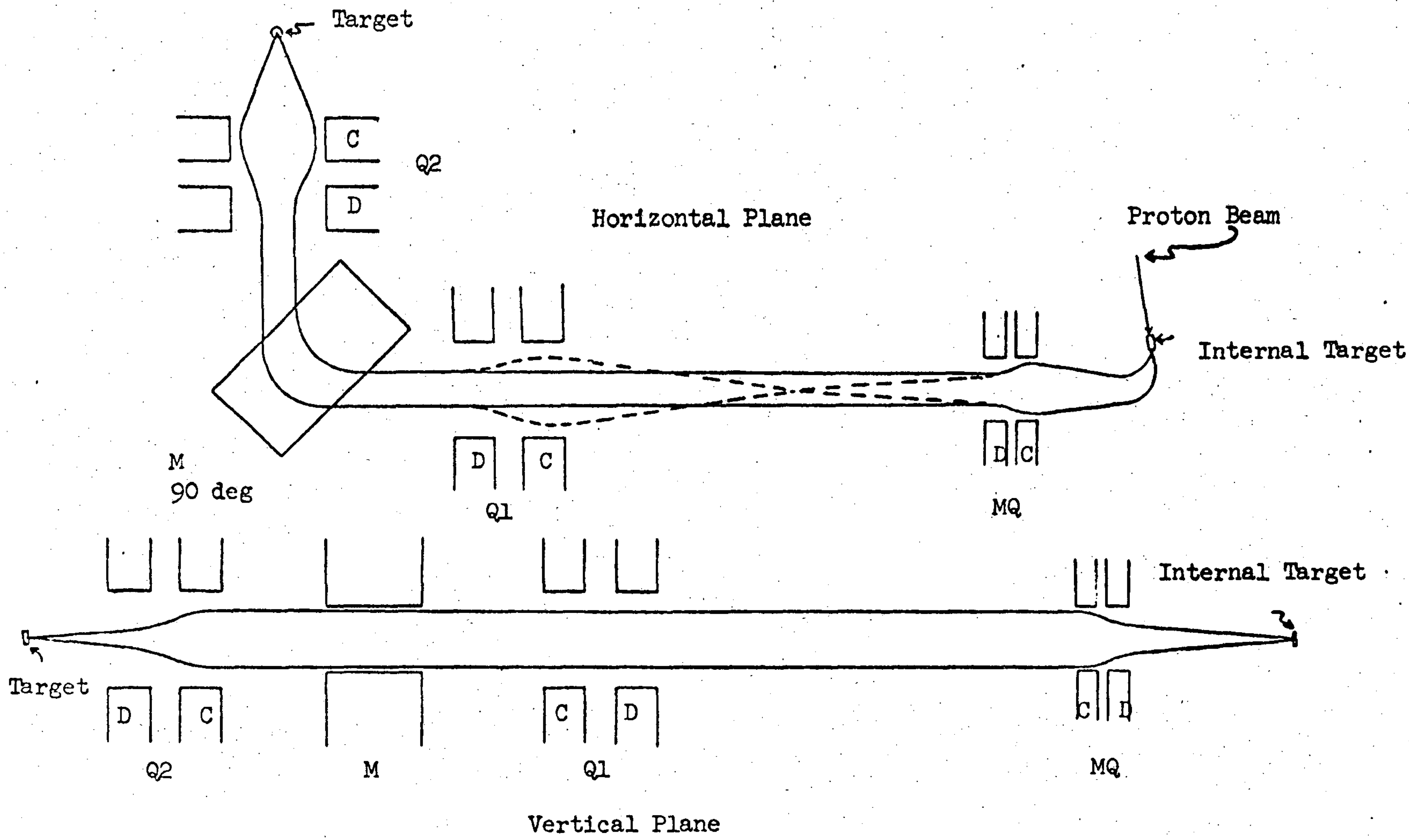

Figure 3. Beam optics for the pion beam.

between MQ and the quadrupole magnet Q1 (see dashed curves in figure 3). Q1 was then used to again form a parallel beam which was focused at the target by Q2. A helium bag was used from the meson wheel (see figure 1) to the end of Q2 in order to reduce the scattering of the beam which affects both the focusing properties and the intensity of the beam.

The following techniques were used to determine the magnet currents and internal target position. The quadrupole currents and the internal target position were first calculated with the computer programs OPTIK[27] and Cyclotron Orbits.[28] The current needed in the bending magnet to deflect 242 MeV/c pions by 90 degrees was established by the wire orbit technique.[29] These settings were checked and adjusted experimentally. Three scintillators in coincidence were used to measure the flux of particles at the ^{3}He target position. The dispersed beam was tuned first. The internal target was positioned where calculated with the Cyclotron Orbits program. The currents in M and Q2 were set at the calculated values and MQ and Q1 were not used at this time. Q2 was then adjusted to give a maximum coincidence rate. Note that since Q2 was so far from the pion source, the beam was nearly parallel at the entrance of Q2 and not using MQ did not appreciably affect the focusing conditions for Q2. The current in MQ was then set to the calculated value and readjusted experimentally to give a maximum beam flux. This occurs when MQ is adjusted to produce a parallel beam. The internal target position and the quadrupole currents were varied slightly to ensure that the optimum settings were obtained. To tune the beam for a momentum focus at the target, Q2 was left at the current setting determined for the dispersed beam and MQ and Q1 were set to the values calculated with OPTIK for a focus midway between MQ and Q1. A slight adjustment of all three quadrupoles was necessary to achieve the maximum beam flux. An integral range curve was taken to check that the desired beam energy had been attained.

The beam composition was determined with an integral range curve and found to consist of $60 \pm 10\%$ π^-, 15% μ^- and 25% e^-. The pion flux was 2×10^5 π^-/sec. with E = 140 MeV and ΔE = ±3 MeV and $.6 \times 10^5$ π^-/sec. with E = 140 MeV and ΔE = ±1.5 MeV.

C. Target

The overriding consideration in the design of the target was the expense of the ^{3}He and necessity that all of the ^{3}He be retained.[30] This meant that the ^{3}He had to be contained in a closed system. The target consisted of two separate systems, the liquid helium coolant and the ^{3}He flask and gas reservoir, with the condenser their only point of contact (see figure 4). The condenser had two sections which were physically separated but thermally connected. A metering-valve regulated the flow of liquid helium into the condenser in which a partial cacuum was maintained. The vacuum lowered the temperature of the helium below the boiling point of ^{3}He, cooling and liquifying the ^{3}He which was collected in the flask. It was also possible to use ^{4}He in the ^{3}He system. This was done to check the target and the rest of the experimental apparatus before the ^{3}He was added.

The amount of material that the incident beam and the scattered particles must pass through at the target determines how much unwanted scattering takes place. For this reason the material surrounding the ^{3}He was made as thin as possible. A cross sectional view of the target assembly in the region surrounding the flask is shown in figure 5. The flask was a cylinder four inches high and four inches in diameter with a stainless steel top and bottom and sides of .0075 in. mylar. Around the flask were two heat shields, one at liquid nitrogen temperature and the other at liquid helium temperature. Each of the shields consisted of .0005 in. of aluminum and .00025 in.

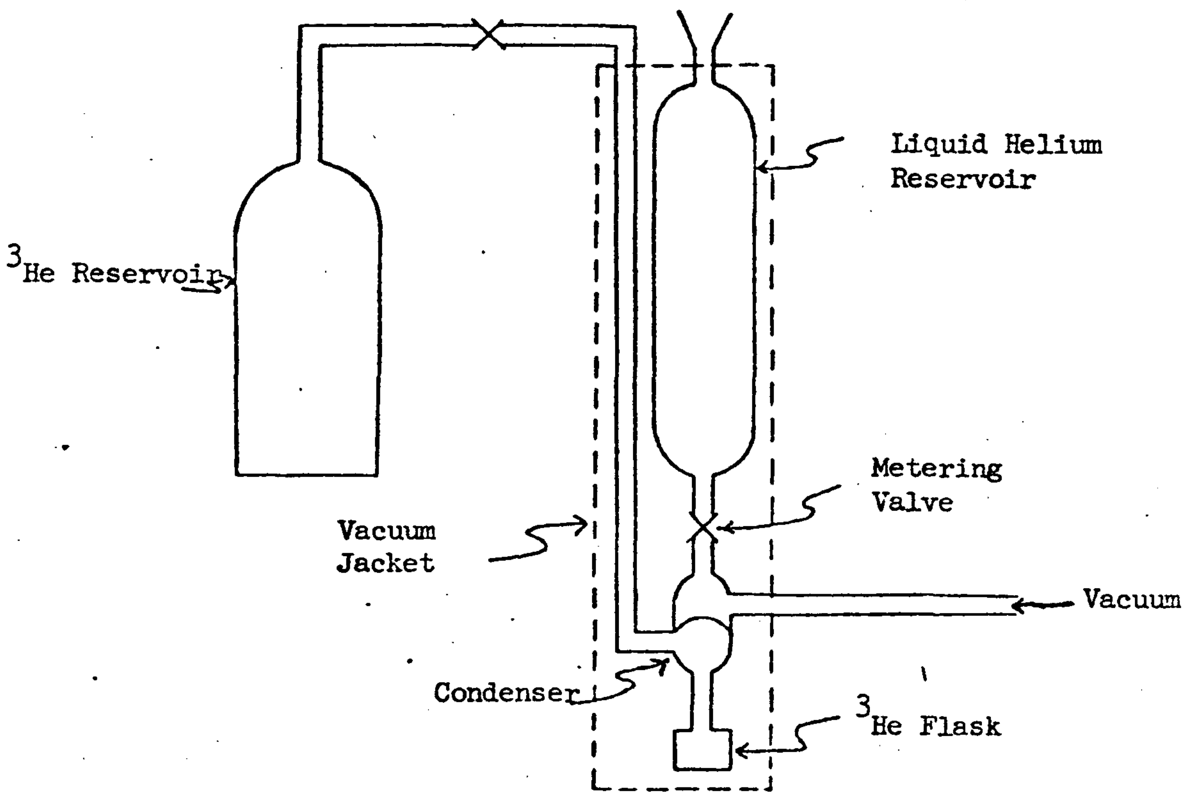

Figure 4. Schematic diagram of the target assembly.

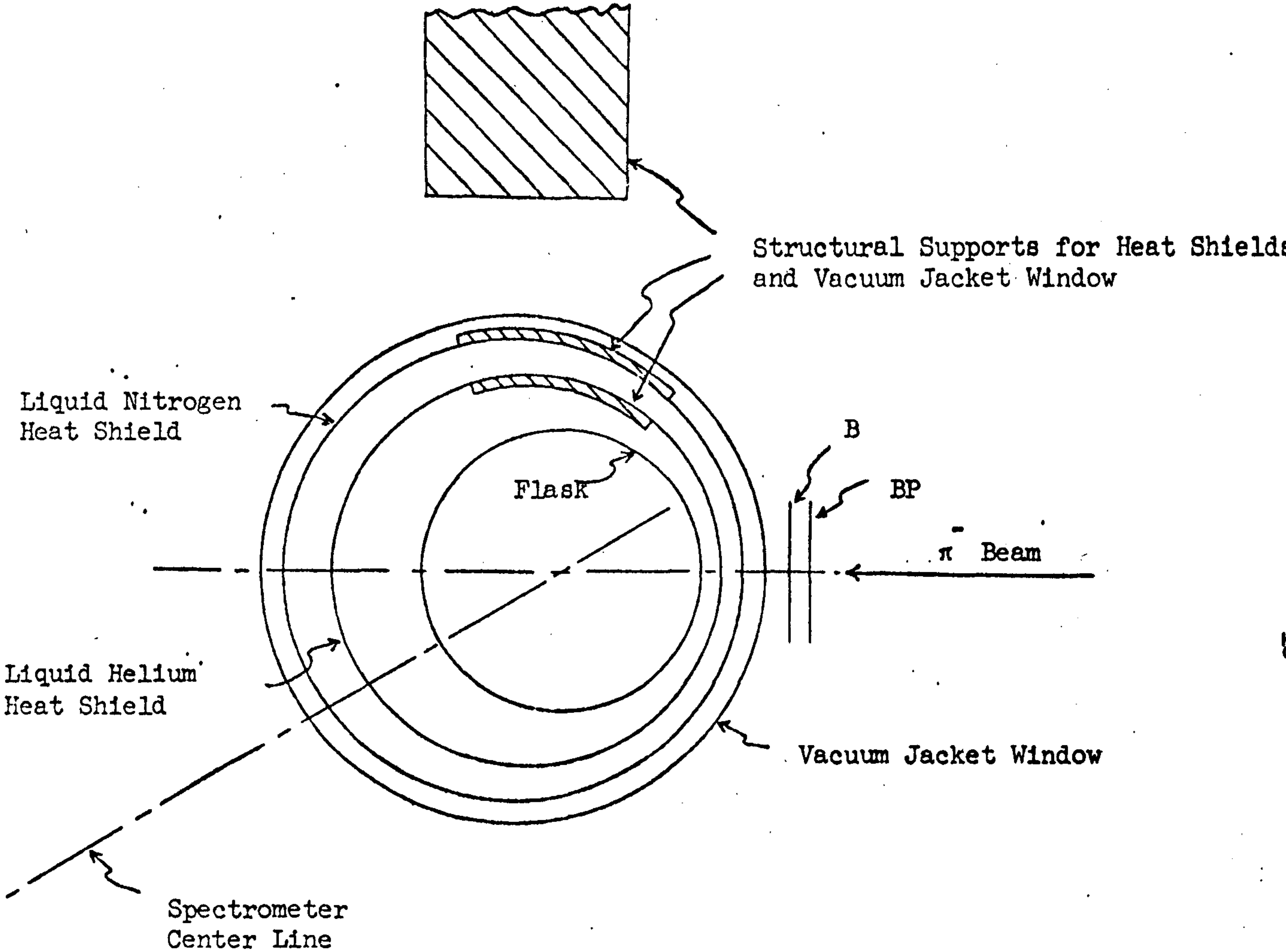

Figure 5. Target cross section showing the flask, heat shields, and entrance window. The flask was off center so that the beam monitor counters could be as close as possible to the target.

of aluminized mylar in the region surrounding the flask. The entire target assembly was maintained in a vacuum to prevent heat loss to the target. There was a .0175 in. mylar window where the beam entered and the scattered particles excited the target assembly. This window was thick so that it would be strong enough to contain the ^{3}He inside the vacuum jacket should the flask break.

Since the density of the liquid ^{3}He varies with temperature it was necessary to monitor the temperature in the flask. Carbon resistors, for which the resistance as a function of temperature had been measured, were mounted in the flask and served as the temperature monitor. The operating temperature was generally 1.7° K, corresponding to a liquid ^{3}He density of .08 gm/cm^3. The target-empty data was taken with the flask evacuated.

D. Magnetic Spectrometer

Figure 6 is a schematic diagram of the wire-chamber spectrometer. The magnetic field was produced by a 16 x 36 in. BeV "C" magnet with the pole tips modified to a size of 25 x 36 in. to give a uniform field over a larger area. This produced an average bend of 90° over the range of particle momenta from 60 to 260 MeV/c. The vertical separation between the pole tips was 8 in. A 2-in. slab of iron with a gap of 8-in. was placed on both the entrance and exit sides of the magnet to reduce the extent of the fringing field. This reduced the fringing field enough so that the only significant bending of the particle trajectories occurred in the region between chambers 2 and 3. The vertical component B_z of the magnetic field was measured in the midplane of the magnet ($z = 0$) and at $z = \pm 2.5$ in. Measurements were recorded on a .5 in. by 1.0032 in. horizontal grid. The values of B_z, $\frac{\partial B_z}{\partial x}$, $\frac{\partial B_z}{\partial y}$ on the midplane and at $z = \pm 2.5$ are obtained by interpolation of the measured values of B_z. The three components of the field at any position are computed by using the Maxwell equations $\vec{\nabla} \cdot \vec{B} = 0$ and $\vec{\nabla} \times \vec{B} = 0$, the boundary condition $B_x(x,y,0) = B_y(x,y,0) = 0$, and the above interpolated values.[31] A more complete description of the field calculating routine is given in Appendix A.

There were four wire spark chambers in the spectrometer, two on either side of the analyzing magnet. Since only three chambers were needed to compute the momentum of a particle, the fourth chamber overdetermined the momentum and allowed the rejection of pion decays

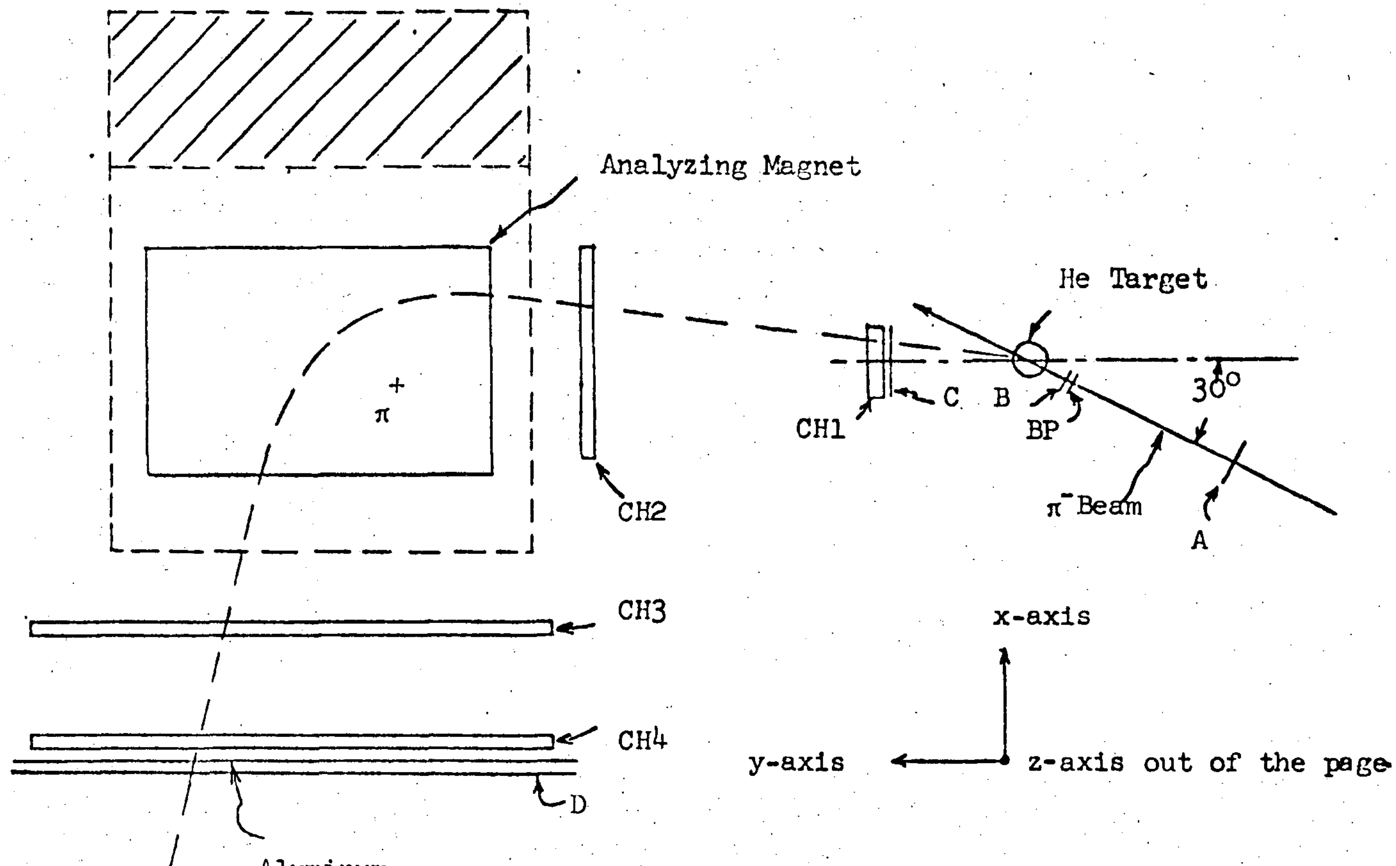

Figure 6. Spectrometer setup.

in flight, scattering from the magnet pole tips, and spurious tracks produced by two different particles. The chambers had the following active areas: chamber (1) 8 x 8 in., (2) 18 x 22 in., (3) and (4) 15 x 55 in. All chambers had four wire planes. In chambers (1) and (2) there was a horizontal plane, a vertical plane and two planes at 45° with respect to the vertical. Chambers (3) and (4) had two vertical planes and two planes at 30° with respect to the vertical. In these two chambers the horizontal coordinate determined the particle momentum. Since the vertical position was not important for the momentum determination some accuracy in the vertical direction was sacrificed for simplicity of construction. A gas mixture of 90% Ne - 10% He with 5 mm of Hg of ethyl alcohol as a quenching agent was circulated through the chambers. A clearing field of 50 V was used to sweep away charged particles and reduce the sensitive time of the chambers. The positions of the sparks were determined by the magnetostrictive-readout technique.[32] Additional information on the construction and performance of the spark chambers is contained in Appendix B.

Behind the fourth spark chamber was a .5 in. thick sheet of aluminum. Protons and pions having a range of .5 in. of aluminum have a momentum of 330 MeV/c and 85 MeV/c respectively. Since the momentum range of interest was from 60 to 260 MeV/c no protons or higher mass particles could have contributed to the data.

Counters C and D detected the passage of a particle through the spectrometer. C was made as thin as possible (1/32 in.) to reduce scattering. The D counter consisted of a set of six scintillators in two rows of three each. The double thickness of counters provided a coincidence and thus rejected tube noise and particles which went through a single counter.

E. Counters and Electronics

Scintillation counters were used in the pion beam to monitor the beam and to determine the incident pion direction and in the spectrometer to detect scattered particles passing through the spectrometer. The positions of the scintillation counters are shown in figure 6. There were three sets of counters (A, B, and BP) in the beam. The four individual A counters each had a sensitive area of 1.5 x 6.0 in. They were overlapped in pairs to define six .75 x 6.0 in. regions. The three B counters were overlapped in pairs to define five .25 x 2.0 in. regions. The active areas of the individual B counters were: B1 and B3 - .5 x 2.0 in. and B2 - .75 x 2.0 in. The same 1.25 x 2.0 in. region was also covered by the counter BP. All the beam counters were made of 1/32 in. plastic scintillator to minimize scattering. The A and B counters determined the direction of the incoming particle to ±1.5 degrees in the horizontal direction. Particles passing through the spectrometer were detected by the C counter and the D counters. The dimensions of the C counter are 3.0 x 7.0 in. and it was made of 1/32 in. thick plastic scintillator to minimize scattering. The six D counters were made of .25 in. thick plastic scintillator. Two of them were 12 x 18 in. and the other four were 24 x 18 in. They were arranged in two rows of three each to form a sensitive region 18 x 60 in. All scintillators were coupled by Lucite light pipes to photomultiplier tubes of type RCA 8575 for A, B, BP and C and type RCA 6810A for the D counters.

Figure 7 is a simplified block diagram of the fast logic electronics used in the experiment. The signals from the four A counters were mixed as were those from the three B counters. The beam was monitored with a triple coincidence A · B · BP. The accidental counting rate was measured by forming a triple coincidence with BP out of time by 208 nsec which corresponds to four cyclotron rf cycles. The signals from the three D counters in each row were mixed and then a double coincidence, $(D_1 + D_2 + D_3) \cdot (D_4 + D_5 + D_6)$, was formed to provide the D signal. The requirement for an event trigger was a signal from D, C, and the beam monitor, (A · B · BP · C · D). This coincidence signal set a gate which disabled the logic for 150 msec., triggered the high voltage pulse to the spark chambers, and strobed a set of flip-flops to accept the signals from the individual A and B counters. The event trigger was also sent to our tape drive unit which then recorded the fixed data and event number, interrogated the flip-flops to see which of them had been set, and recorded the magnetostrictive wand data (see Appendix B for a discussion of the magnetostrictive readout technique).

The stretched-beam spill of the cyclotron consists of a spike of particles 64 times per second followed by an approximately uniform flux for about 10 msec. The spike was gated off since the flux in this part of the beam spill was too high for our electronics to register properly.

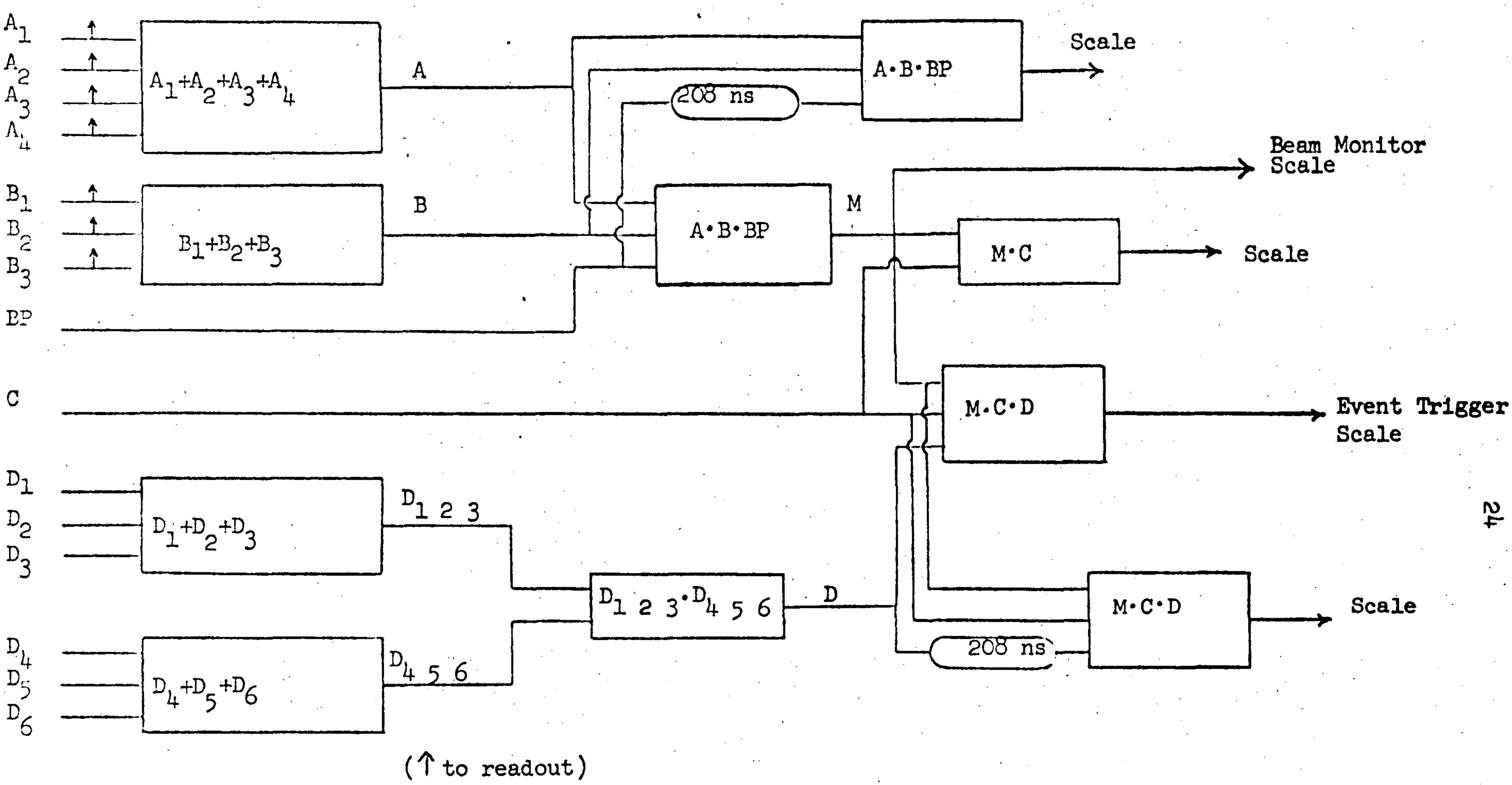

Figure 7. Simplified logic diagram.

A record was kept of the following coincidences: The beam monitor, (A · B · BP), and A · B · BP with BP 208 nsec out of time, (A · B · BP · C), the event triggers, (A · B · BP · C · D), and A · B · BP · C · D with D 208 nsec out of time. Live time was also measured by scaling the pulses from a free running 1 MHz pulse generator when the electronics was gated on. The numbers for a typical double-charge-exchange run are shown in Table 1.

Table I. Scaler numbers for a DCX run

Quantity Scaled	Number of Coincidences
A · B · BP	5081×10^6
A · B · BP(acc)	1242×10^5
A · B · BP · C	5995×10^4
A · B · BP · C · D	32586
A · B · BP · C · D (acc)	13791
Time (sec)	17986

F. Running Conditions

The spectrometer could be set to detect π^-, which was used for $\pi^- + {}^3He$ elastic and inelastic scattering, or π^+, which was used for the double-charge-exchange reaction. Changing from one mode to the other was accomplished by switching the current polarity in the analyzing magnet. Data were taken with the flask both full and empty. For the target empty runs, the flask was evacuated and thus no corrections to the data were necessary for gas remaining in the flask.

Data were also taken with targets of carbon and ${}^4He$ for calibration purposes.

III. DATA ANALYSIS

A. General

The data analysis consists of taking the experimentally measured quantities and from them extracting the missing mass distributions in the reactions $\pi^- + {}^3He \rightarrow \pi^\pm + X$. The mass of the recoiling particle X is given by:

$$M_X^2 = 2m^2 + M^2 + 2M(E_b - E_s) - 2E_bE_s + 2P_bP_s\cos\theta \qquad (1)$$

where m is the pion mass, M is the ^3He mass, E_b is the energy of the beam particle, E_s is the scattered pion energy, P_b is the beam momentum, P_s is the scattered pion momentum, θ is the scattering angle, and M_X is the mass of $\left\{ {ppn \atop nnn} \right\}$ system. The speed of light c is everywhere equal to one. The quantities P_b, P_s, and θ were determined with the experimental data. The experimental data which were recorded on magnetic tape for each event consisted of: 1) bookkeeping entries which included the tape number, the file number, the event number, the target status (full or empty), the target material (^3He or ^4He), and the spectrometer polarity, and 2) the actual scattering data which included the combination of individual A and B counters present in the event trigger and the digitized spark information from each magnetostrictive wand. Provisions were made to record two spark positions for each wand.

A computer program used these data to reconstruct each event. The digitized wand information was used to compute the spark positions in the chambers. The counter data and the sparks in the first two chambers determined a plane and a line whose intersection was the interaction point in the target and whose angle of intersection was the scattering angle. The spark locations in the first three chambers were used to obtain the particle momentum. The spark position in the fourth chamber allowed the discrimination against pion decays in flight, spurious sparks in the chambers, and scattering in the spectrometer. The scattered particle energy and the beam energy were corrected for energy loss in the target and the spectrometer, and then used in addition to the scattering angle to calculate the missing mass M_X. In elastic scattering this mass corresponded to the mass of ^{3}He which provided a consistency check of the beam energy.

After weighting each event according to the spectrometer solid angle acceptance and pion decay probability, the events were histogrammed as a function of the missing mass. The positron background to the double-charge-exchange data was estimated by the Monte Carlo technique (see Appendix D) and the final histograms of the data were obtained by subtracting the positron contribution from the experimental data.

A more complete explanation of these calculations is contained in the succeeding sections.

B. Points and Lines

The data consisted of eight numbers for each spark chamber, two numbers for each plane in a chamber. The two numbers indicated either zero, one, or two sparks. Each spark number determined a line or "wire", parallel to the chamber wires, on which the spark was located. A point was found for which the sum of the squares of the distances to the wires was a minimum.[33] For this calculation all chamber planes were assumed to be at the central plane of the chamber. The four chamber planes determined four equations of the form

$$a_i x + b_i z = s_i, \tag{2}$$

or in matrix notation

$$Ar = s, \tag{3}$$

where the a_i and b_i are the elements of the 4×2 matrix A, r is a vector in 2-space, and s is a vector in 4-space. It can be shown that vector r_o defined by

$$r_o = A^I s, \tag{4}$$

where A^I is the generalized inverse of A, is the desired least squares solution. Furthermore if $a_i^2 + b_i^2 = 1$, then the components of the 4-vector d given by

$$d = Ar_o - s = (AA^I - I)s, \tag{5}$$

where I is the identity matrix and d is a vector in 4-space, are the perpendicular distances to the individual wires. The solutions in those cases where data existed in all four planes were called "4-wire fits". A small fraction of the time one of the planes would not have any data, in which case 3-wire fits were obtained by the same method.

The line-finding procedure was very similar to that used in finding points. In this case the objective was to find the line through two chambers with the sum of the squares of the perpendicular distances to all the wires in the two chambers being a minimum. The line in 3-space was represented in the parametric form

$$x = p_1 y + p_2 \tag{6}$$

$$z = p_3 y + p_4 . \tag{7}$$

As before the equation for a wire in the ith plane was

$$a_i x + b_i z = s_i \tag{8}$$

or

$$a_i y_i p_1 + a_i p_2 + b_i y_i p_3 + b_i p_4 = s_i \tag{9}$$

or in matrix notation

$$Ap = s \tag{10}$$

where p is a vector in 4-space, y_i is the y-position of the ith chamber plane, the coefficients of p_i are the elements of the 8 x 4 matrix A, and s is a vector in 8-space. The vector p_o defined by

$$p_o = A^I s \tag{11}$$

is the desired least squares solution and the components of the 8-vector d given by

$$d = Ap_o - s = (AA^I - I)s \tag{12}$$

are the perpendicular distances to the individual wires. Lines were also found by the same method in cases where there were only 6 or 7 wires.

C. Momentum Determination

The information used to calculate the momentum of a particle consisted of three points on the particle trajectory and the known magnetic field. The first two points, which were outside of the magnetic field, fixed the incoming direction of the particle trajectory. The technique for computing the momentum involved estimating the momentum and using it in the equations of motion for the Lorentz force $\frac{d\vec{P}}{dt} = \frac{e\vec{P}}{mc} \times \vec{B}$ and the relationship $\frac{d\vec{X}}{dt} = \frac{\vec{P}}{m}$ where $\vec{P}$ is the vector momentum, $\vec{X}$ is the vector position, $\vec{B}$ is the vector magnetic field, e is the electron charge, m is the relativistic particle mass, and c is the speed of light. These equations were integrated through the magnetic field and the point of intersection (X_3) with chamber 3 was found. If X_3 was close enough to the actual spark location the momentum determination was finished. Otherwise the momentum estimate was improved and again integrated through the magnetic field and this process repeated until the desired accuracy was attained.

Since integration is very time consuming it was important to have a good momentum estimate and a check to see if the three points corresponded to a possible orbit. The momentum estimate and the orbit check was made with the aid of two polynomials P(x1, x2, y3) and Y4(x1, x2, y3) where P is the momentum estimate, Y4 is the y4 position estimate and x1, x2, and y3 are the x and y coordinates of the sparks in chambers 1, 2, and 3 respectively. For the orientation of the coordinate system see figure 6. These polynomials are of the form

$$\Theta = \Sigma a_{ijk}\, x1^{i}\, x2^{j}\, y3^{k} \qquad (13)$$

$$i = 0,1$$
$$j = 0,3$$
$$k = 0,2$$

The coefficients a_{ijk} were obtained by making a least squares fit to a set of orbits which spanned our data space. The resultant polynomials determined the momentum to ±1% in the momentum range of 60 to 250 MeV/c and the position in chamber four to ±.3 in. (see figures 8 and 10).

The actual sequence of computing the momentum was as follows: The spark chamber data consisted of the four points (x1, y1, z1), (x2, y2, z2), (x3, y3, z3), and (x4, y4, z4). The coordinates x1, x2 and y3 were used in the polynomial Y4 to compute the expected y4 coordinate, $y4_e$. If $|y4 - y4_e| > 2$ in. the event was rejected. While analyzing the data a histogram of the difference $y4 - y4_e$ was made for good events and the value of 2 in. was chosen empirically to reject a negligible fraction of the good events. If the event survived the Y4 cutoff, x1, x2, and y3 were used in the momentum polynomial P to estimate the momentum. An orbit was integrated through the field using the estimated momentum and the starting position and direction given by the points (x1, y1, z1) and (x2, y2, z2). The computed orbit intersections with chambers three and four, $(x3_c, y3_c, z3_c)$ and

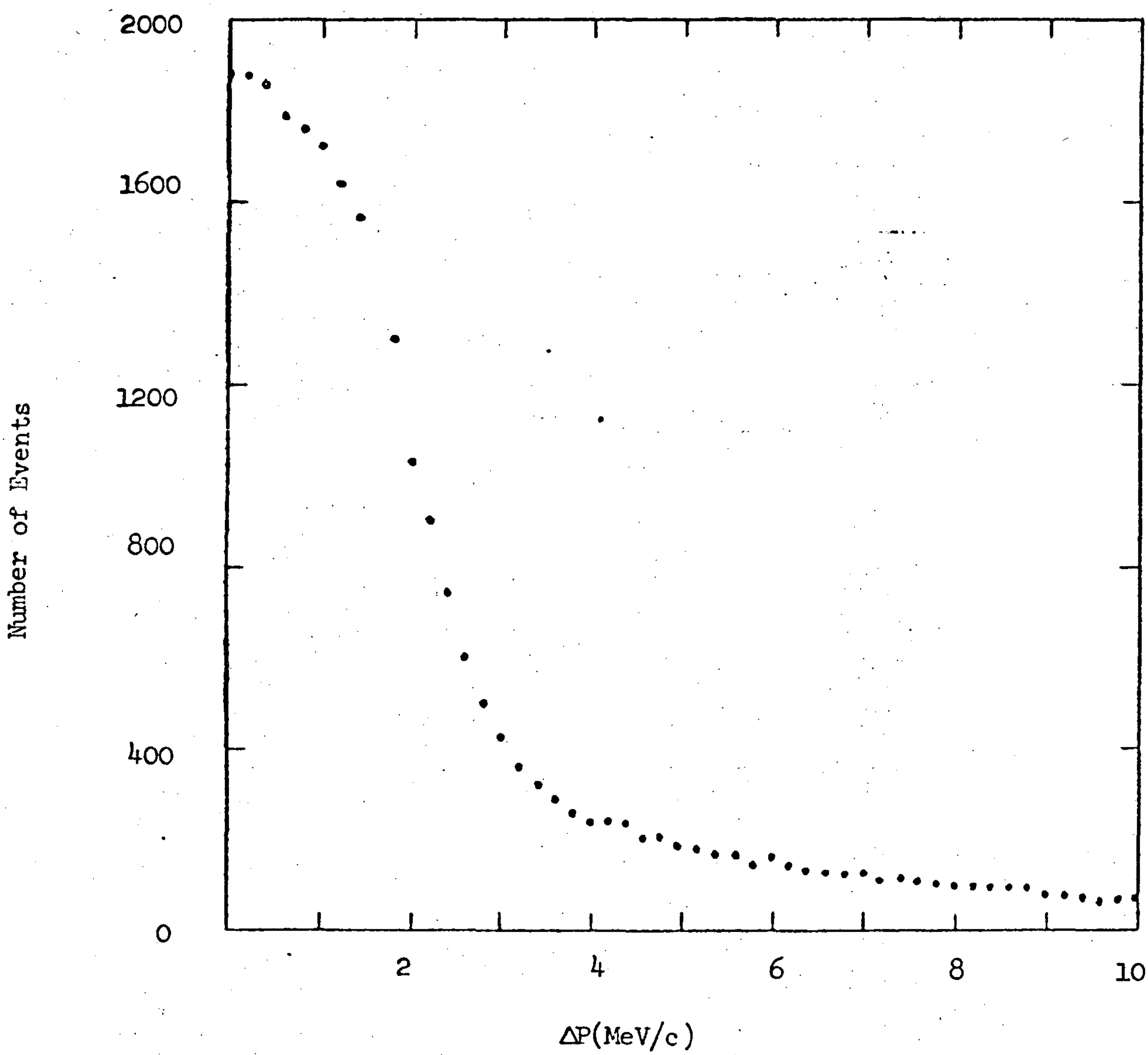

Figure 8. A histogram of the absolute value of the difference between the polynomial momentum estimate and the final iterated momentum.

$(x4_c, y4_c, z4_c)$ were obtained. The momentum estimate was then updated as indicated:

$$P_{new} = P_{old} + P(x1, x2, y3) - P(x1, x2, y3_c) \qquad (14)$$

The integration process was repeated until $|y3 - y3_c| < .05$ in. When this condition has been satisfied, $|P(y3) - P(y3_c)| \lesssim .2$ MeV/c. In practice the y3 condition was satisfied about 15% of the time after the first orbit, 70% of the time after the second orbit and the remaining 15% of the time after the third orbit.

D. A Good Event

The following is a discussion of the event acceptance criteria and the data processing performed at each step in the analysis.

1) The A and B counter arrays must each have had a signal from a single counter or from a pair of overlapping counters. If this condition was satisfied, a vertical plane, constructed to pass through the centers of the regions defined by the counters, was used to represent the direction of the incoming particle. Otherwise the event was rejected.

2) Each spark chamber had to have at least one spark. Points were found by the method discussed in section B. A point was considered an acceptable spark if the perpendicular distance to the "worst wire" (the largest component of the vector d) was less than .25 in. in chambers 1 and 2 and less than .45 in. in chambers 3 and 4. Different tolerances were allowed for the two pairs of chambers since the trajectories of all particles in chamber 1 and 2 made an angle of less than 15 degrees with respect to the normal whereas in chambers 3 and 4 angles of trajectories up to 45 degrees with respect to the normal were considered. All possible combinations of 4-wire and 3-wire fits were tried. If any candidate spark had at least two wires in common with an already acceptable spark, it was assumed to be the same spark. In practice there was usually just one spark in each chamber. In order to be sure that an insignificant fraction of the

data was being lost by not considering 2-wire fits a portion of the data was analyzed in which 2-wire fits were allowed. The number of wires in a spark for 1,000 good events is given in Table II. No correlations of missing wires in one chamber with missing wires in another chamber were observed. Since the absence of a spark in any chamber eliminates an event, rejecting the 2-wire fits decreases the overall efficiency by approximately 2%.

3) The sparks had to lie within certain regions of the chambers. Chambers 2 and 3 were situated close to the iron magnet-shield which had an 8-in. gap, 4-in. above and below the median plane of the magnet. Spark coordinates occurring more than 3.5 inches from the median in chamber 2 or more than 4.5 inches from the median in chamber 3 were discarded, since a particle on a trajectory outside of these regions would strike either the shield or the magnet pole tip. If discarding such a spark meant that a chamber did not have any remaining sparks, the event was rejected.

4) The intersection of a line (determined by sparks in the first two chambers) with a plane (which represents the incident particle direction) had to be within the target volume. For this test, the target was assumed to be a cylinder 2.5 in. high and 4.0 in. in diameter. Events having their intersections outside of this volume were produced by scattering from the B counters, from the heat shields, and from the vacuum jacket surround the target.

Table II. Number of times each chamber had n wires in a spark.

Chamber	Number with n wires in spark n = 4	3	2
1	968	28	4
2	959	37	4
3	961	32	7
4	967	30	3

5) There had to be a "track" in the first pair of chambers (1 and 2). For those events which survived all the previous cuts a line was computed by the method described in section B. For a line to be considered a good track, the perpendicular distance to the worst wire had to be less than .15 in. If this criterion was not satisfied the worst wire was discarded and the line was recomputed. If discarding the worst wire meant that chamber had less than three wires remaining the event was rejected. Figure 9 shows a typical histogram of the wire-to-track deviation for a chamber plane. As is apparent from the figure the wire-to-track deviation is usually less than .02 in.

6) Tracks through chambers 3 and 4 had to make an angle of less than 45 degrees with respect to the normal to these chambers. At large angles the spark tends to jump straight across the gap in a random manner instead of following the particle path (see Appendix B). Thus the spark location accuracy deteriorated with large angles. The cutoff angle of 45 degrees was chosen to include most events and yet reject those for which the particle trajectory was inaccurately determined.

7) The spark in chamber 4 had to be within 2 in. of the point predicted by the Y4 polynomial. This test discriminated against background events produced by pion decay in flight, scattering in the spectrometer, or spurious sparks in the chambers. A histogram of the deviation $y4-y4_e$, where y4 is the spark position in chamber 4 and $y4_e$ is the expected position in chamber 4 computed with the Y4 polynomial,

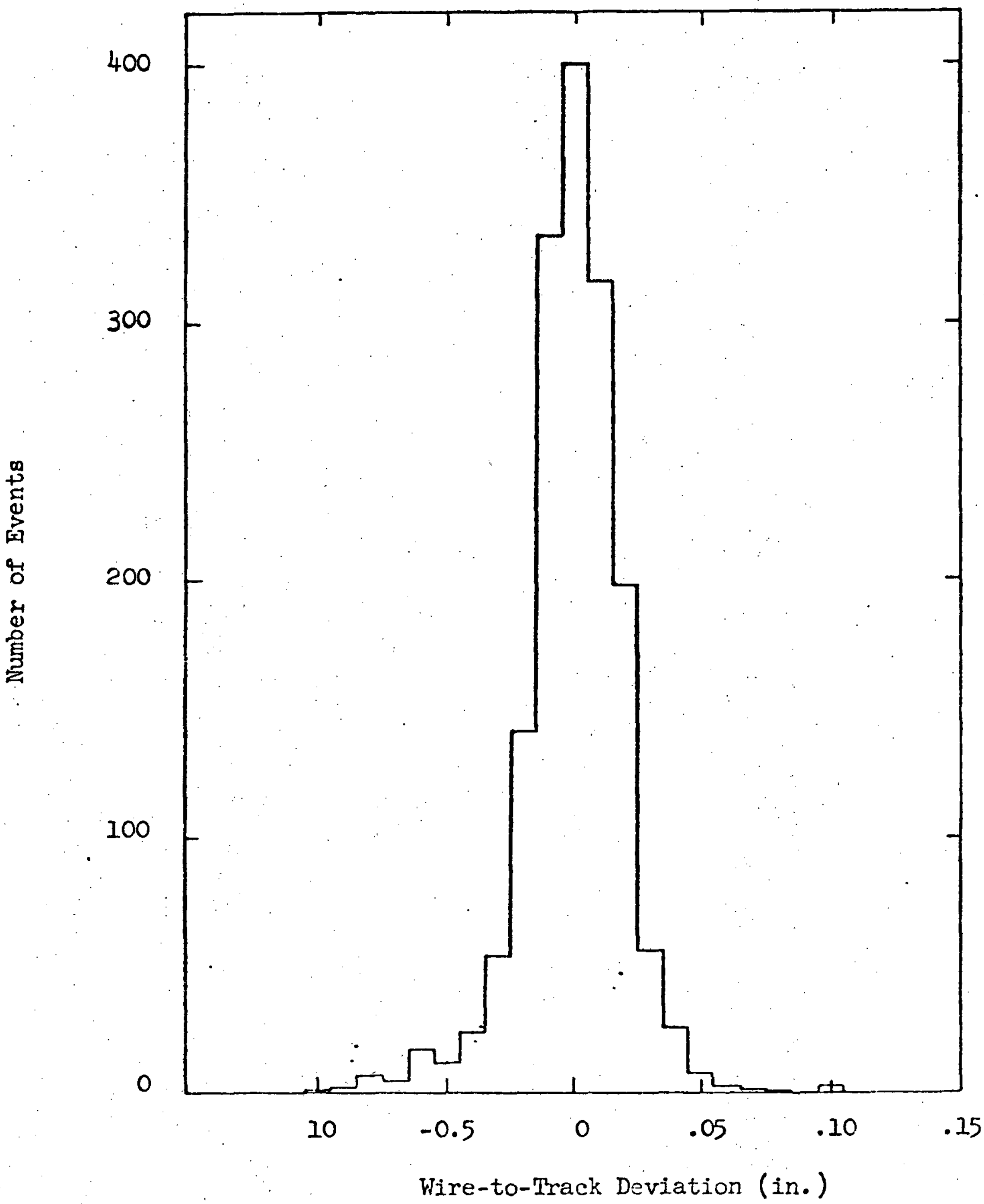

Figure 9. A histogram of the wire-to-track deviation for a set of tracks determined by 4-wire fits in two chambers.

is shown in figure 10 for the double-charge-exchange good events. As can be seen from the figure, the 2-in. cutoff rejected a neglibible fraction of the good events.

8) There had to be a track in the last pair of chambers (3 and 4). Again, the requirement was that the perpendicular distance from the worst wire to the line, determined as described in section B, be less than .15 in.

9) The particle trajectory had to miss the magnet pole tips. The analyzing magnet had an 8-in. gap, 4-in. above and below the median plane. The integration was stopped immediately if at any point in the magnet the orbit position was greater than 4.5 in. from the median plane. The cutoff was made large in case the momentum estimate, and therefore the orbit position, was incorrect. On the final integration of the trajectory, events having a maximum deviation from the median plane greater than 3.5 in. were rejected.

10) The events had to originate in a target volume which was a cylinder 2-in. high and 3-in. in diameter. Since the uncertainty in the scattering position was approximately .35 in., events for which the computed scattering position was within .5 in. of the flask walls were rejected. This cutoff rejected those events which originated in the target walls. The 2-in. vertical dimension was chosen to correspond to the 2-in. height of the B counters in the beam monitor.

11) The angle between the computed orbit and the track in

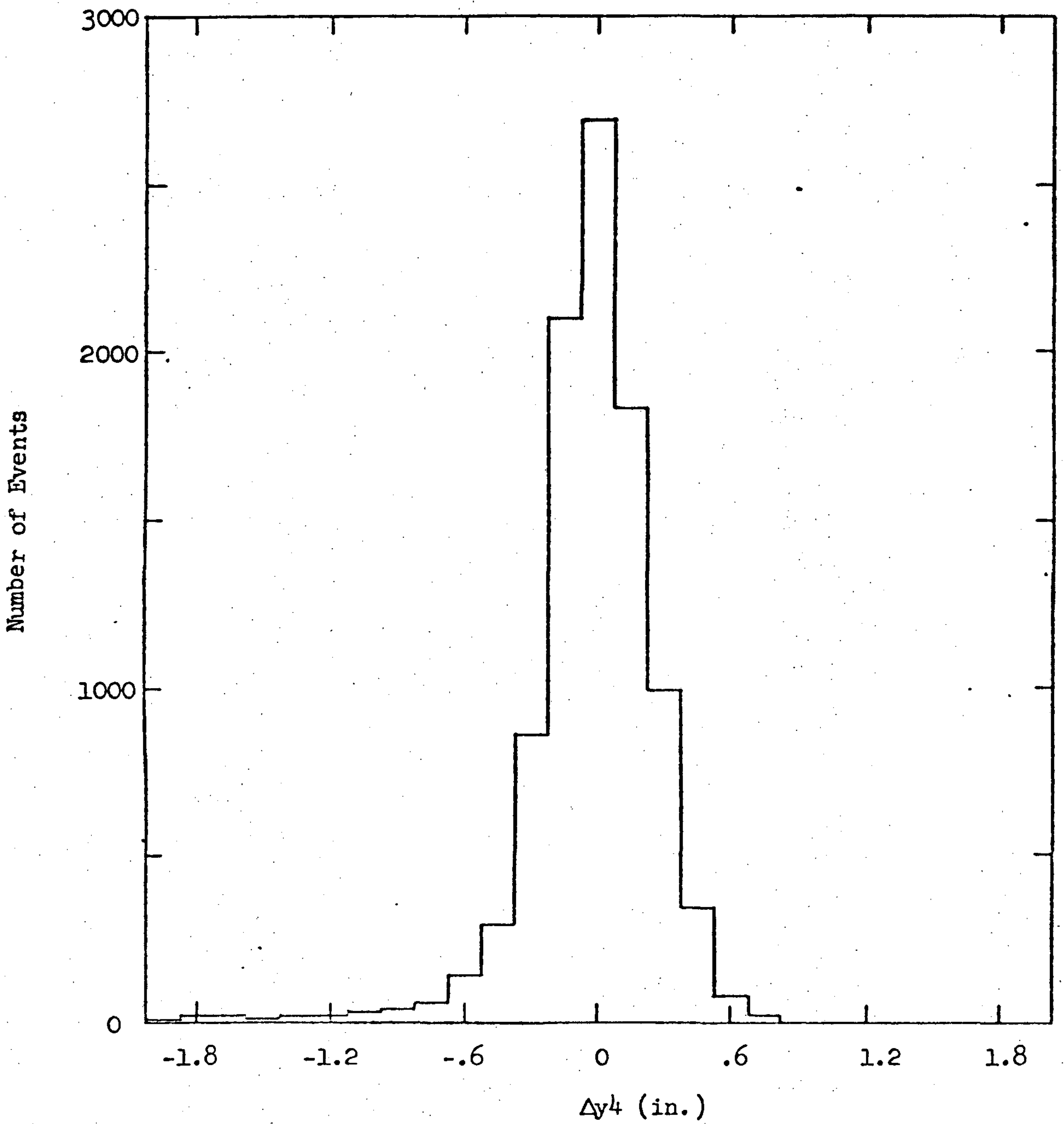

Figure 10. A histogram of the difference between the polynomial estimated y4 position and the actual y4 position for the double-charge-exchange events.

chambers 3 and 4 had to be small. The requirements were: $\Delta H \leq .012/\sqrt{P}$ and $\Delta V \leq .012/\sqrt{P} + .02$ (where P is the particle momentum in BeV/c) and ΔH (ΔV) is the tangent of the horizontal (vertical) projection of the angle between the computed orbit and the track. The factor $\sqrt{P}$ in the denominator of ΔH was determined empirically to fit the width of the resultant angular deviations and reflects the fact that multiple scattering is greater for lower momentum particles. The acceptable vertical deviation was much larger than the acceptable horizontal deviation since both the spark chambers and the magnetic field were designed to give the greatest accuracy in the horizontal direction. Figure 11 shows the distribution of ΔH for particles of momentum .240 BeV/c.

Table III shows the fraction of events rejected by each of the above checks for the elastic scattering data and for the double-charge-exchange data. In the DCX reaction about 75% of the events did not have sparks in all the chambers. Most of these events were accidental coincidences between the D counters and the rest of the triggering logic. Since the trigger rate was only approximately 1 per second and since these events were easily rejected in the data analysis, no attempt was made to decrease the fraction of accidental triggers. About 50% of the events having sparks in all four chambers originated outside of the target volume in both of the above reactions. Such events were due to scattering in the B counters, and heat shields and vacuum jacket surrounding the flask.

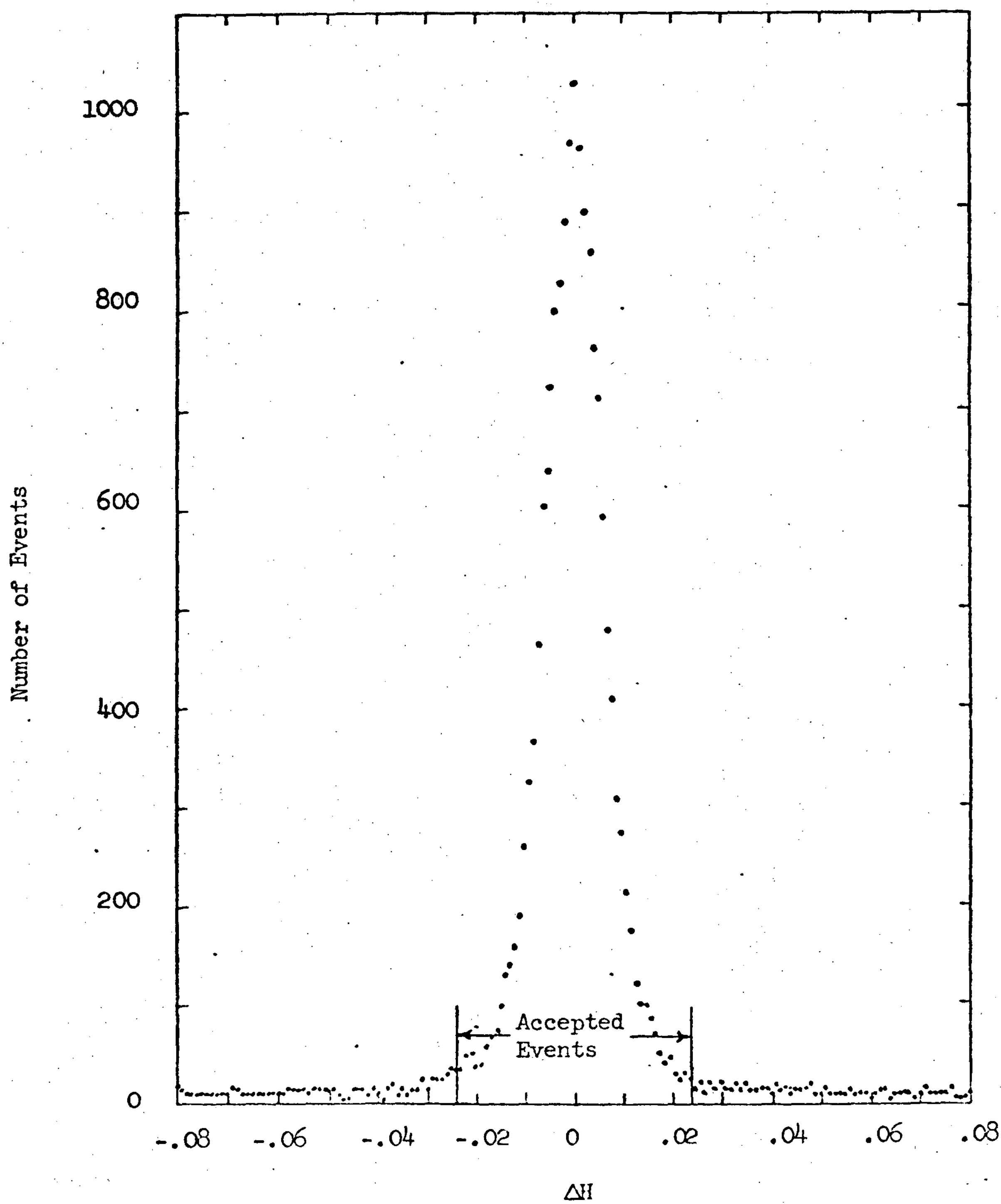

Figure 11. A histogram of the tangent of the horizontal angle between the computed orbit and the track given by chambers three and four. The accepted "good" events are indicated.

Table III. Fraction of events rejected by the event acceptance criteria.

Cutoff	Elastic Reject	Elastic Remain	Double-Charge-Exchange Reject	Double-Charge-Exchange Remain
1) Logic	.049	.951	.114	.886
2) Sparks	.071	.880	.744	.142
3) Spark out	.028	.852	.020	.122
4) Target intersect	.468	.382	.091	.031
5) Tracks in	.004	.379	.002	.030
6) > 45 deg out	.003	.376	.002	.028
7) Y4 deviation	.028	.348	.012	.016
8) Tracks out	.002	.346	.000	.016
9) Pole tips	.085	.261	.004	.012
10) Target 11) Orbit checks	.089	.170	.005	.007

E. Errors and Corrections

1) Energy loss in the target and spectrometer.

For a fixed beam energy E_{ob}, the energy E_b at the scattering position was given by

$$E_b = E_{ob} - \frac{dE_b}{dx} L_b \tag{15}$$

where $\frac{dE_b}{dx}$ is the pion stopping power and L_b is the path length in the target. Similarly the energy of the scattered pion E_s at the scattering positron was given by

$$E_s = E_{os} + \frac{dE_s}{dx} (L_s + L_{sp}) \tag{16}$$

where E_{os} is the scattered pion energy as determined with the spectrometer, L_s is the path length in the target, and L_{sp} is the path length to chamber 2 in the spectrometer excluding the target.

2) Uncertainty in the energy.

The energy resolution was limited by the following: Energy spread of the beam, multiple scattering in the spectrometer, uncertainty in scattering angle, and uncertainty in the scattering position. The energy uncertainty of M_X was obtained by the standard formula:

$$\langle \Delta M_X^2 \rangle^{\frac{1}{2}} = \left[\left(\frac{\partial M_X}{\partial E_{ob}}\right)^2 \Delta E_{ob}^2 + \left(\frac{\partial M_X}{\partial E_{os}}\right)^2 \Delta E_{os}^2 + \left(\frac{\partial M_X}{\partial \theta}\right)^2 \Delta \theta^2 + \left(\frac{\partial M_X}{\partial L}\right)^2 \Delta L^2 \right]^{\frac{1}{2}} \tag{17}$$

with M_X given by equation (1). To first order, the partial derivatives are as follows:

$$\frac{\partial M_X}{\partial E_{ob}} = (M - E_s + \frac{E_b}{P_b} P_s \cos\theta) \cdot \frac{1}{M_X} \qquad (18)$$

$$\frac{\partial M_X}{\partial E_{os}} = (-M - E_b + \frac{E_s}{P_s} P_b \cos\theta) \cdot \frac{1}{M_X} \qquad (19)$$

$$\frac{\partial M_X}{\partial \theta} = (-P_b P_s \sin\theta) \cdot \frac{1}{M_X} \qquad (20)$$

$$\frac{\partial M_X}{\partial L} = \left[\frac{dE_b}{dx} \, (-M - E_s + P_s \frac{E_b}{P_b} \cos\theta) \right.$$

$$\left. + \frac{dE_s}{dx} \, (M - E_b + P_b \frac{E_s}{P_s} \cos\theta) \right] \cdot \frac{1}{M_X} \qquad (21)$$

In determing equation (21) the relationship $dL_b \cong - dL_s$ was used.

The numerical values of the uncertainty in M_X were computed by evaluating the above expressions for the partial derivatives and entering the experimental uncertainties. Over the range of angles and scattered-pion energies of this experiment,

$$\left| \frac{\partial M_X}{\partial E_{ob}} \right| \cong \left| \frac{\partial M_X}{\partial E_{os}} \right| \cong 1.$$

Figure 12 and 13 show the variations of $\left|\frac{\partial M_X}{\partial \theta}\right|$ and $\left|\frac{\partial M_X}{\partial L}\right|$ as a function of M_X. The uncertainties in the beam energy and the scattering location were nearly constant for all scattered-pion energies and angles. The values (FWHM) were: $\Delta E_{ob} \cong 6$ MeV or $\Delta E_{ob} \cong 3$MeV and $\Delta L \cong .4$ in. The uncertainty in the energy of the secondary pion as determined with the spectrometer was due mainly to multiple scattering in the spectrometer. The effects of multiple scattering were estimated to produce deviations with respect to an orbit in a vacuum of the order of .25 in. at chamber 3. This is to be compared with the spark location accuracy of ± .02 in. The energy uncertainty was computed using the estimated uncertainty due to multiple scattering and the known momentum variation as a function of position in chamber 3. The results are shown in figure 14. The uncertainty in the scattering angle was a result of the finite width of the individual A and B counters and the multiple scattering of the incident and secondary pion in the target and counters. The total uncertainty in the scattering angle is shown in figure 15. Finally, figure 16 shows the total energy uncertainty in M_X as a function of M_X.

2) Event weight.

Each event was given a weight which was a function of its momentum and path length through the spectrometer. The factor $4\pi/\Omega$ (p) corrected for the variation of the solid angle acceptance of the spectrometer as a function of the momentum p. A graph of $\Omega(p)$ is

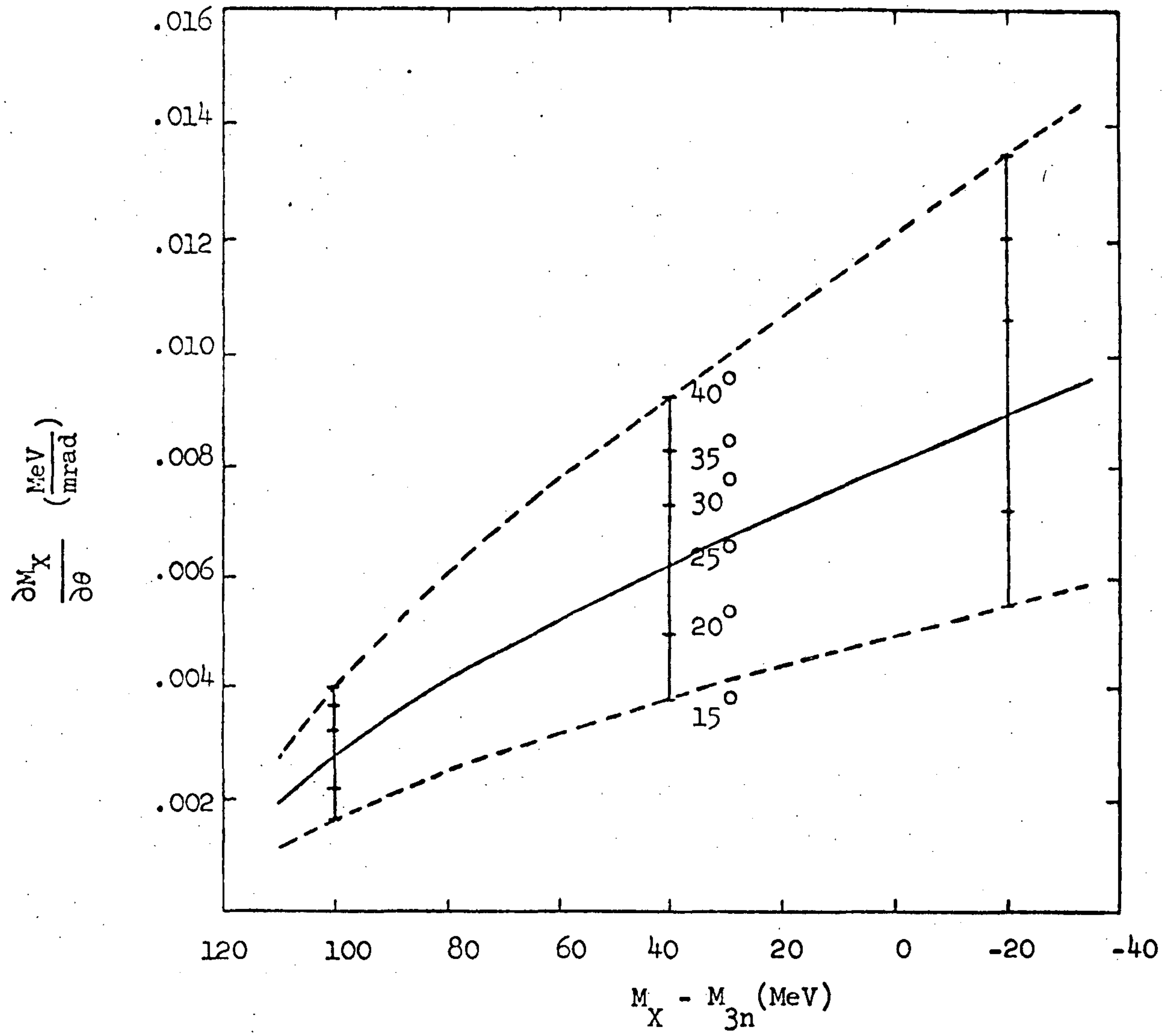

Figure 12. The variation of the missing mass with respect to a change in the scattering angle. Curves are given for different values of the scattering angle. Zero on the abscissa corresponds to the mass of three neutrons.

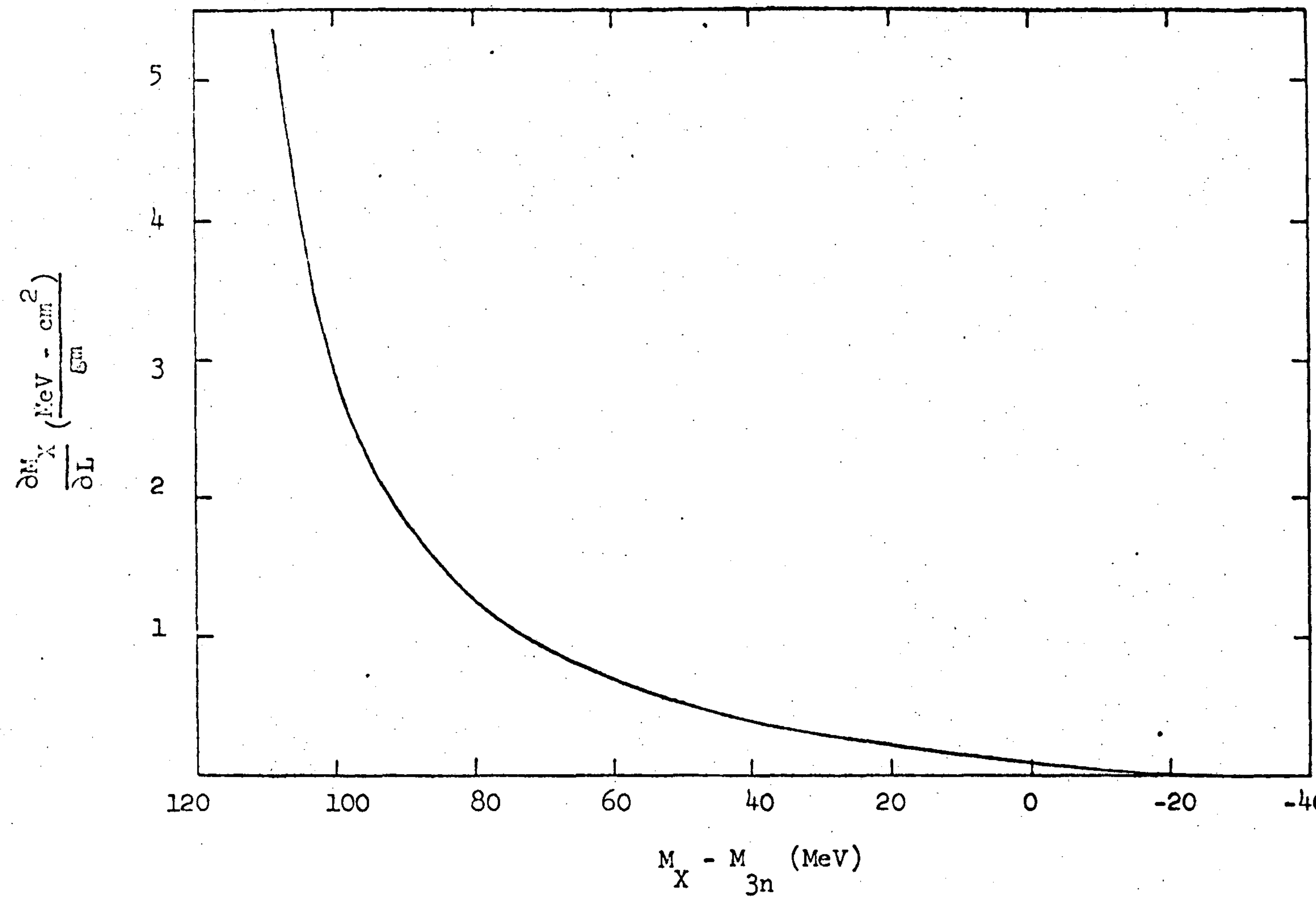

Figure 13. The variation of the missing mass with respect to a change in the scattering position in the target.

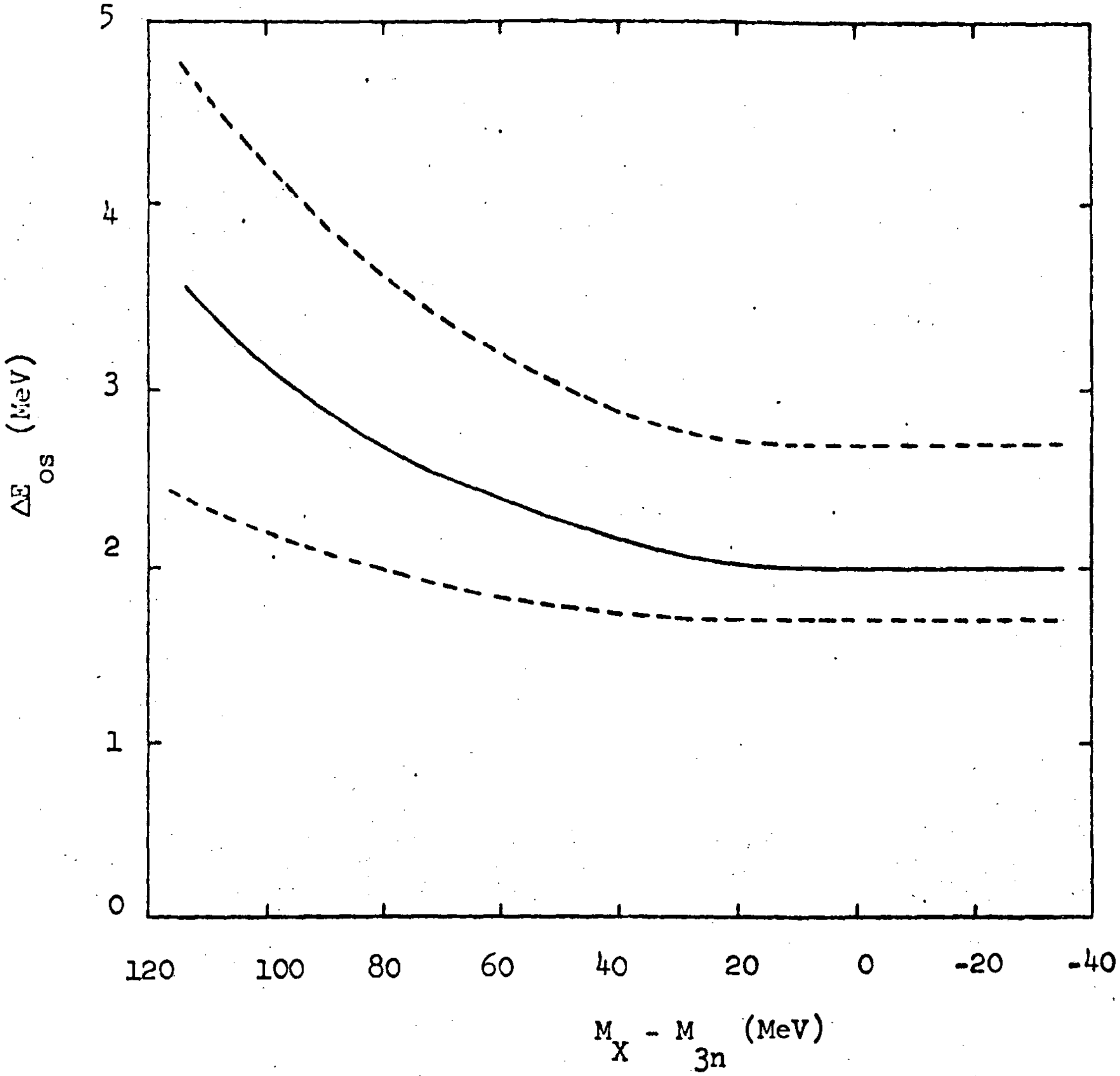

Figure 14. The energy resolution of the spectrometer. The solid line is the resolution for the most probable bending angle in the spectrometer. The dashed line are the resolution for the extreme bending angles which were accepted.

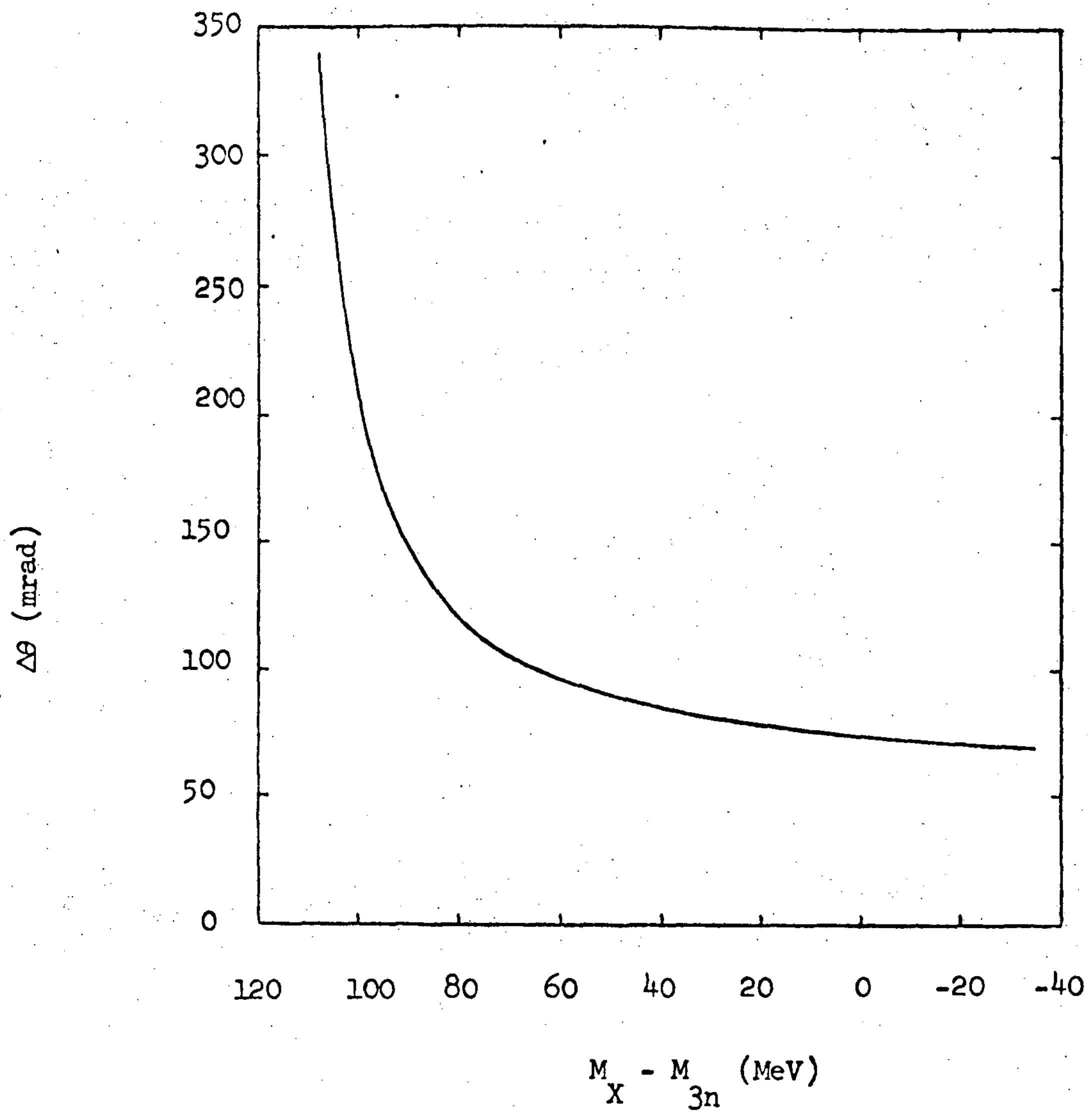

Figure 15. The uncertainty in the scattering angle.

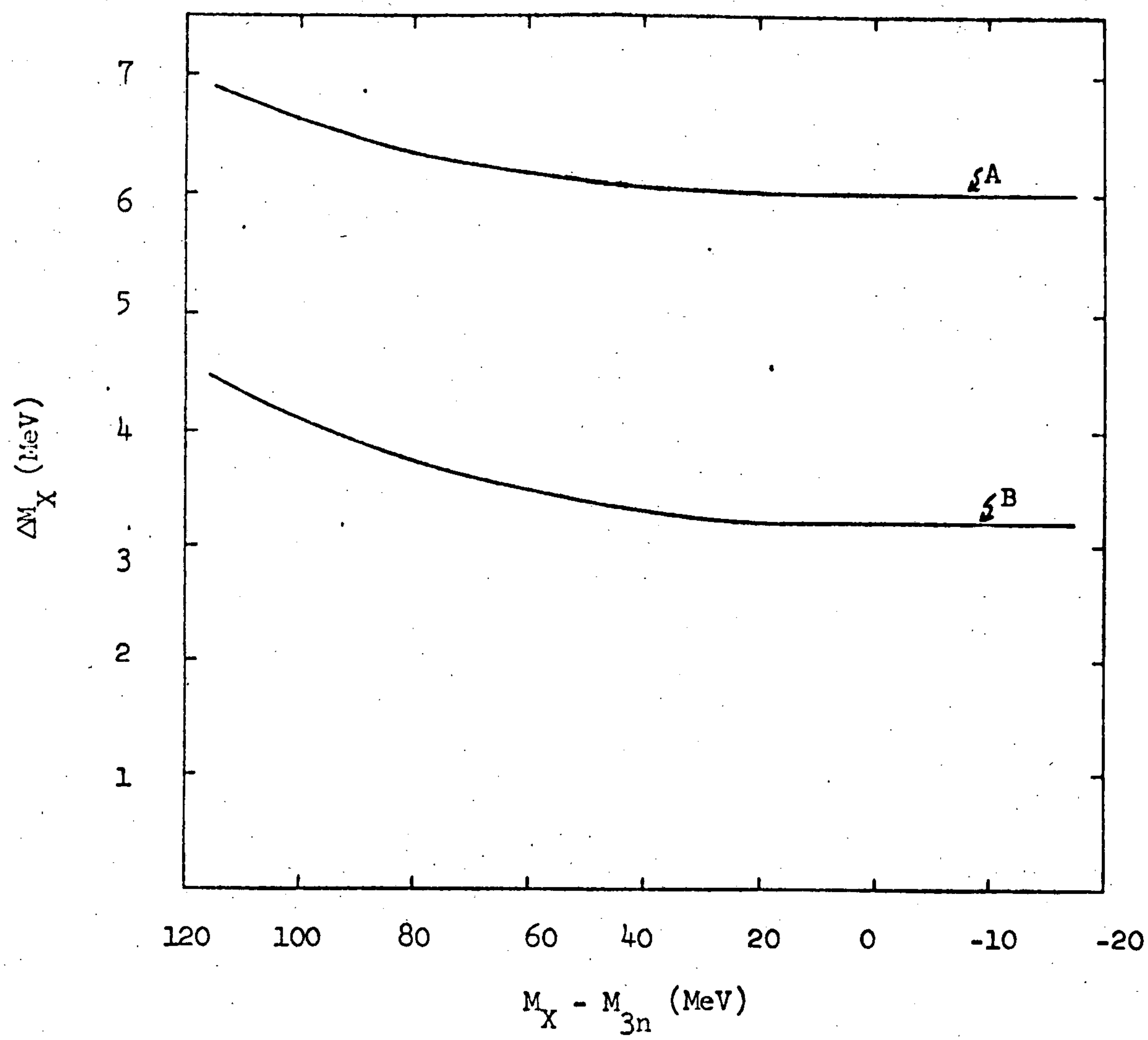

Figure 16. The energy uncertainty in the missing mass. Curve A is the result for the momentum focused beam. Curve B is the result for the dispersed beam.

shown in figure 2. A description of the Monte Carlo calculation to determine $\Omega(p)$ is given in Appendix C. The solid angle acceptance is adjusted about ten per cent to convert to the solid angle acceptance in the center of mass. The second factor in the event weight corrected for pion decays in flight in the spectrometer and was of the form $\exp\left(\frac{mD}{P_s\tau}\right)$ where m is the pion rest mass, D is the path length through the spectrometer, P_s is the particle momentum, and τ is the pion lifetime.

3) Background

A source of uncertainty in the data was the percentage of pion decays which survived all our cuts on the data and appeared to be good events. This fraction has been estimated by the Monte Carlo method to be about 3% (Appendix E). These events consisted almost entirely of pions which scattered in the target and then decayed between the target and the first spark chamber.

The double-charge-exchange data also contained a background of positrons. As stated earlier, particles triggering our system had a range of greater than .5 in. of aluminum, plus .25 in. of plastic scintillator. This corresponds to the range of a 90-100 MeV/c pion, depending on the angle of incidence. All events with a momentum of less than 97.5 MeV/c were assumed to be positrons produced in the reaction

$$\pi^- + {}^3\mathrm{He} \rightarrow \pi^0 + pnn$$
$$\pi^0 \rightarrow \gamma e^+ e^-$$

The momentum distribution of positrons produced in the above reaction was computed by the Monte Carlo technique. For the details of the calculation see Appendix D. The normalization was obtained by fitting the calculated momentum distribution to the data in the momentum range of 60 to 97.5 MeV/c. With this normalization the three neutron energy distribution was computed assuming that the positrons were pions and this distribution was then subtracted from the data.

IV. EXPERIMENTAL RESULTS

A. Double-Charge-Exchange

A histogram of the raw data as a function of momentum is shown in figure 17. The computed positron spectrum is also given in the same figure. Figure 18 is a histogram of the data as a function of the three neutron invariant mass. These data are corrected for spectrometer solid angle acceptance, and pion decay in flight. The error bars indicate counting statistics. There is an additional ten per cent uncertainty in the overall normalization as a consequence of the uncertainty in the pion beam flux. In figure 19 the results are shown as a function of the three-neutron invariant mass after subtracting the positron contribution. There is no subtraction for target empty runs since the relative number of good events from target empty runs is negligibly small. In figure 20 the results are divided into two angular bins covering scattering angles of approximately 20°-30° and 30°-40°.

The cross section normalization was checked using the carbon elastic scattering data. A differential cross section of 90 ± 10 mb/sr was measured for elastic scattering on carbon at 30 degrees. This is in good agreement with previous results of 104 ± 6 mb/sr at 150 MeV[34] and 60 ± 15 mb/sr at 125 MeV.[35]

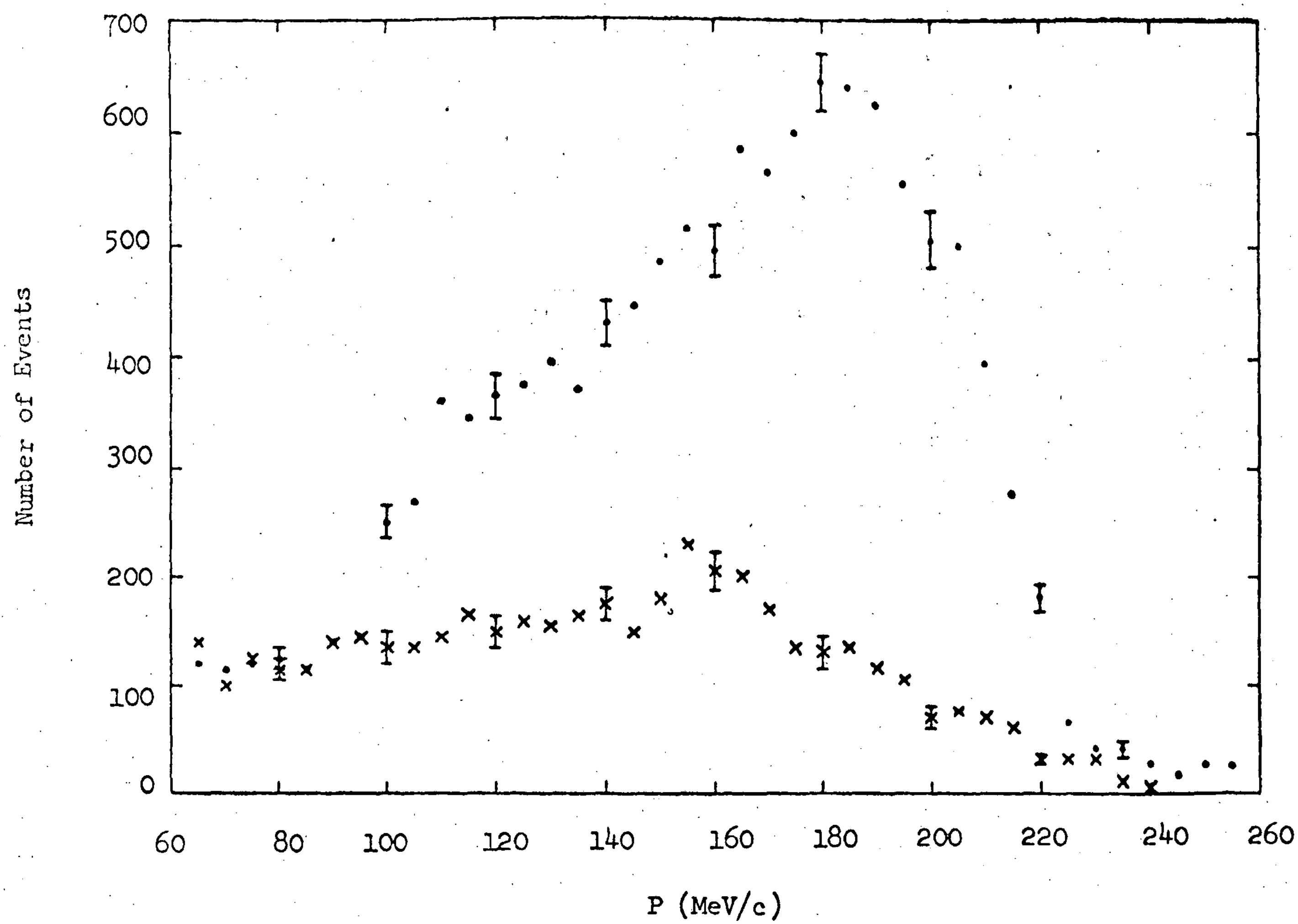

Figure 17. Momentum spectrum of the accepted DCX events. The dots are the experimentally measured data. The crosses are the computed positron data normalized to the experimental data with momenta less than 97.5 MeV/c.

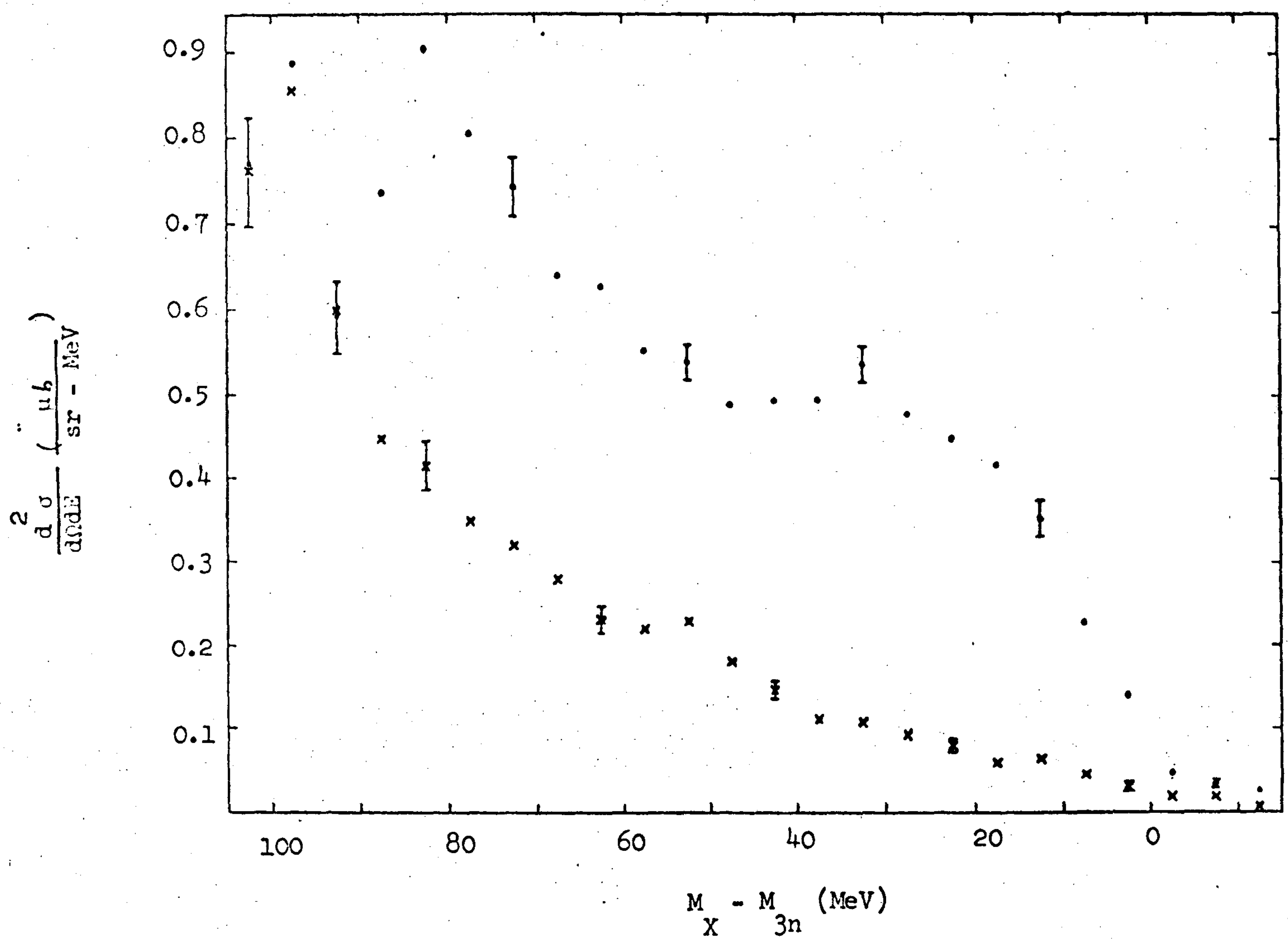

Figure 18. Energy spectrum of the accepted DCX events. The dots are the experimentally measured data. The crosses are the computed positron data normalized as in figure 17.

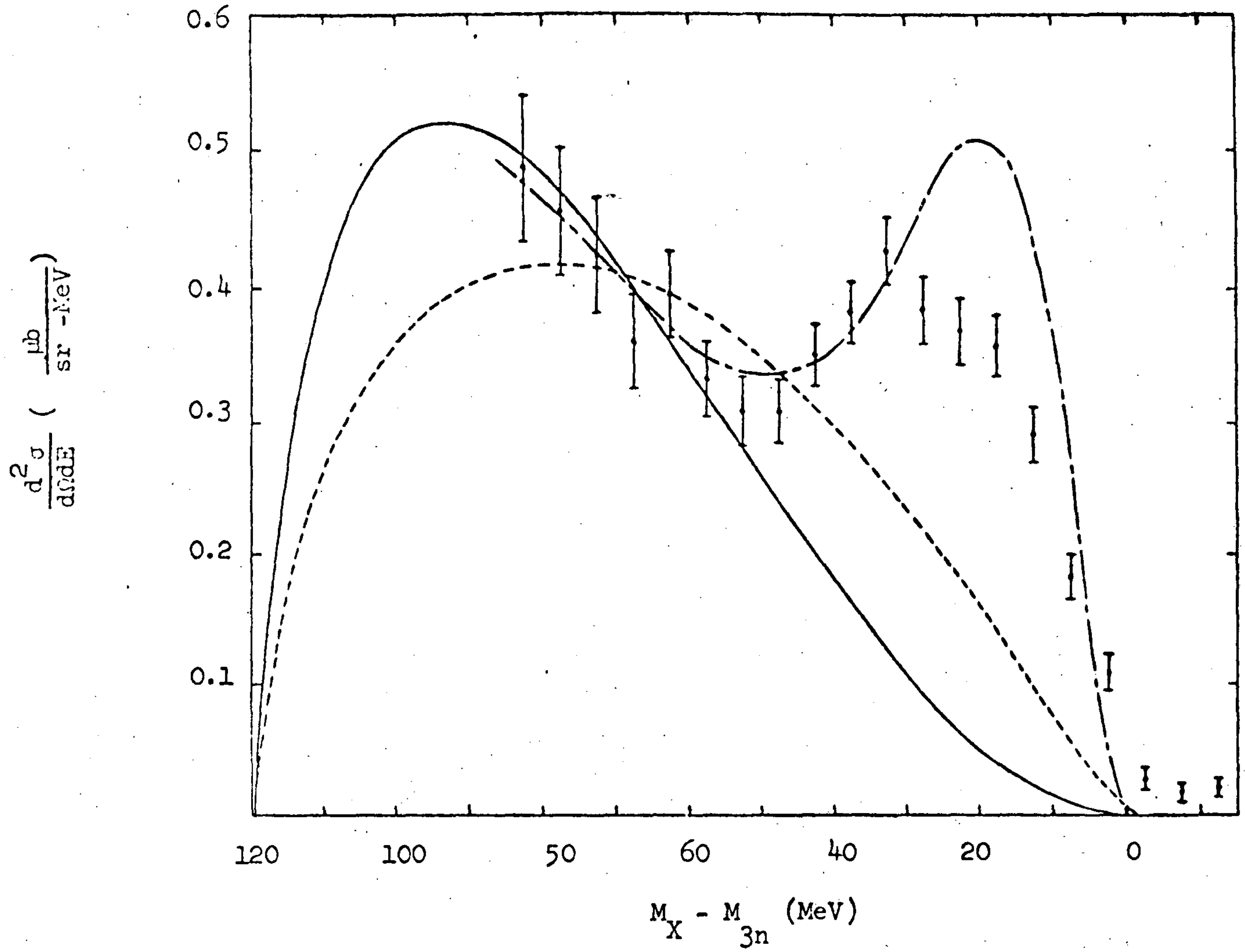

Figure 19. Energy spectrum of the DCX reaction after subtracting the positron background. The solid curve is 4-body phase space and the dashed curve is 4-body phase space distorted by a ^1S_o interaction between two of the neutrons. Both curves are normalized to the experimental data in the energy range of 50 to 85 MeV. The dot-dashed curve is the result of a calculation by Phillips.

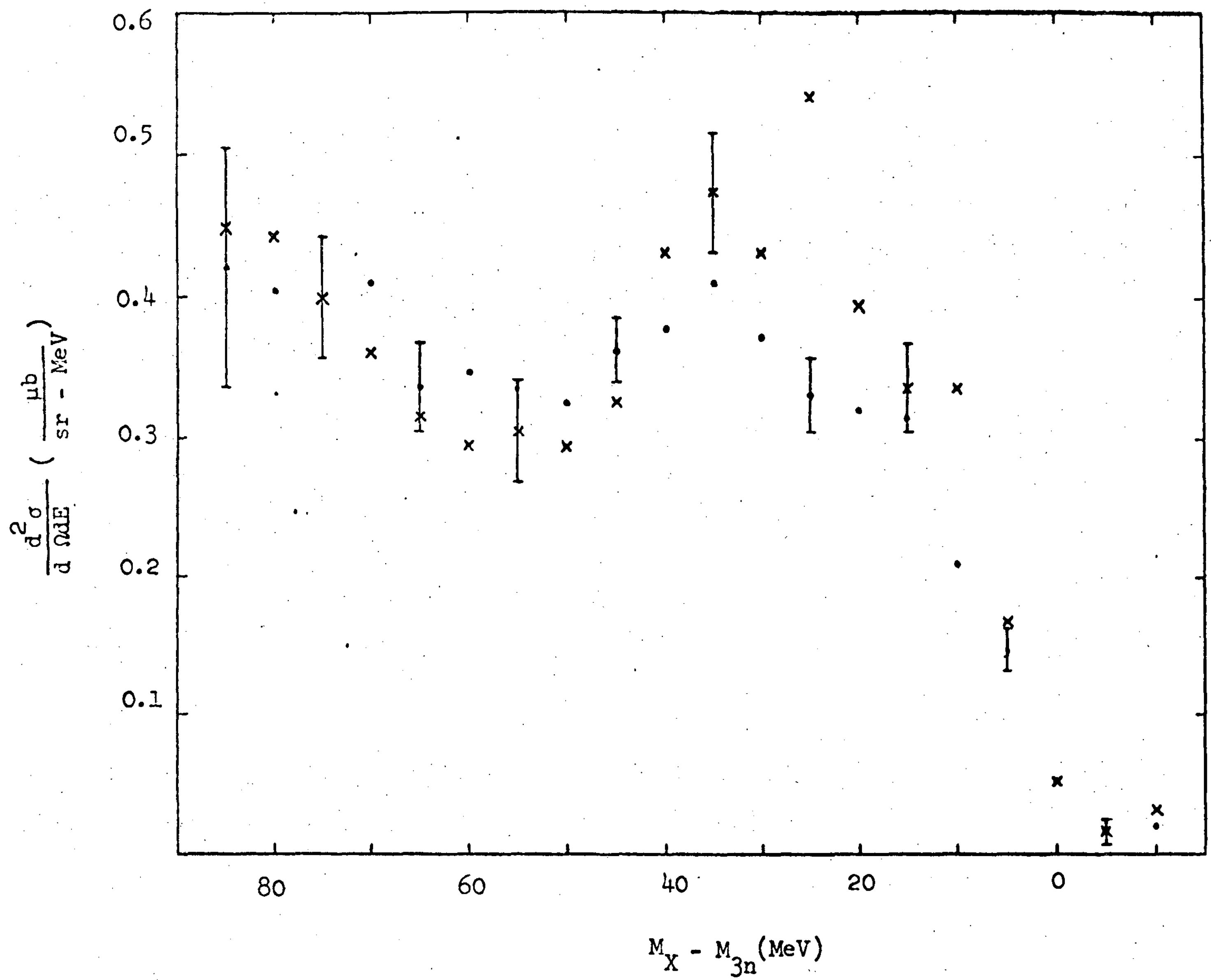

Figure 20. The energy spectrum for the DCX reaction divided into two angular bins. The crosses are for scattering angles in the range of 30 to 40 degrees, and the dots are for scattering angles in the range of 20 to 30 degrees. The angular ranges are only approximate and there is some overlap of the two sets of data.

B. Elastic and Inelastic Scattering

Figure 21 is a plot of the elastic scattering data as a function of the invariant mass of the ppn system. This data is corrected for spectrometer solid angle acceptance and pion decay in flight. In figure 22 the results are presented after subtracting the target empty data. The solid curve is the ^4He scattering data and is normalized to have the same elastic scattering peak height that the ^3He data has. The ^4He elastic scattering peak is extrapolated to zero (the dashed curve) and subtracted from the ^3He data. The results are shown in figure 23.

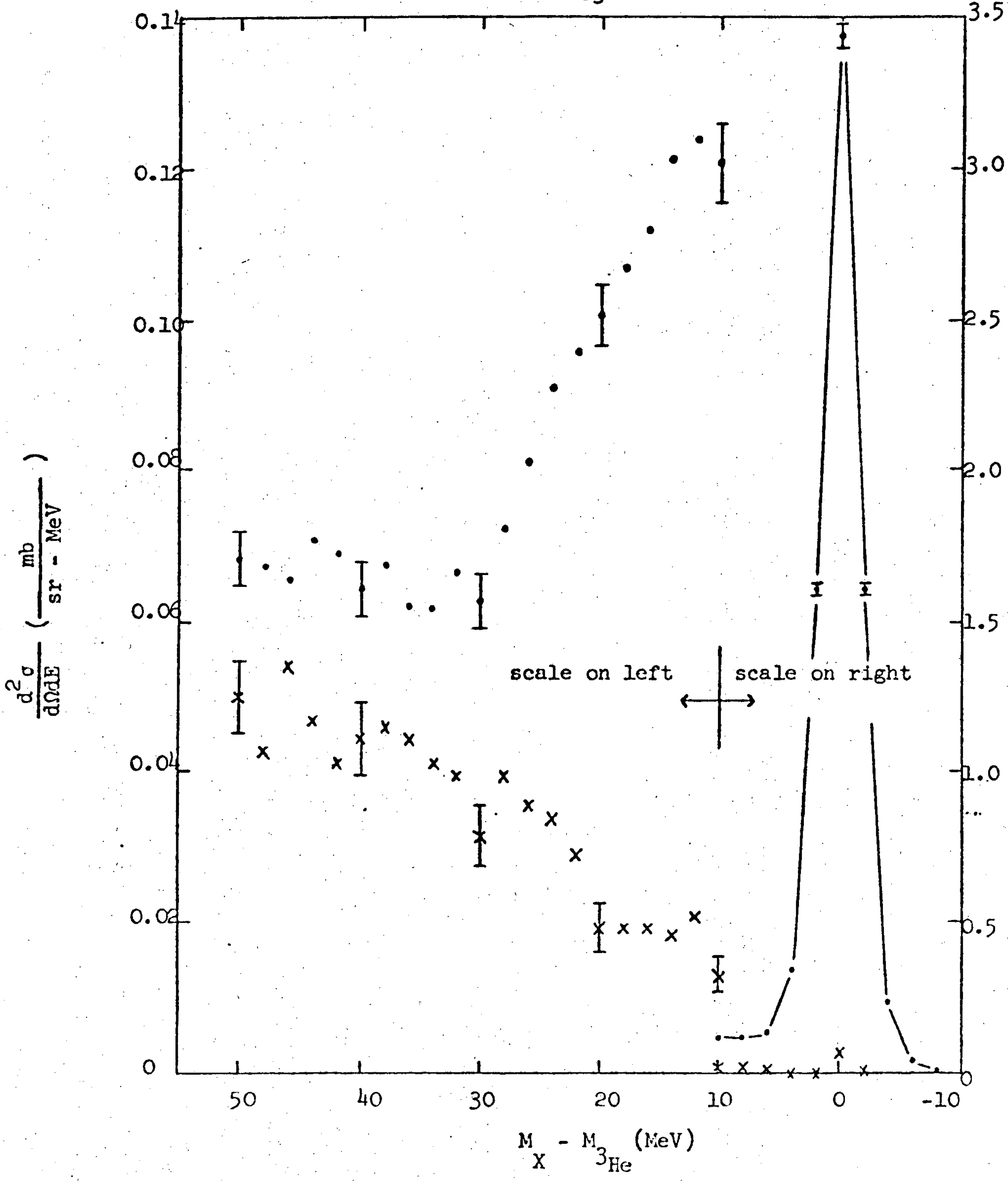

Figure 21. The energy spectrum of the ^{3}He elastic and inelastic scattering data. The dots are the target full data and the crosses are the target empty data. The solid lines connecting the points in the elastic scattering peak are only an aid to the eye. Note the scale change at 10 MeV.

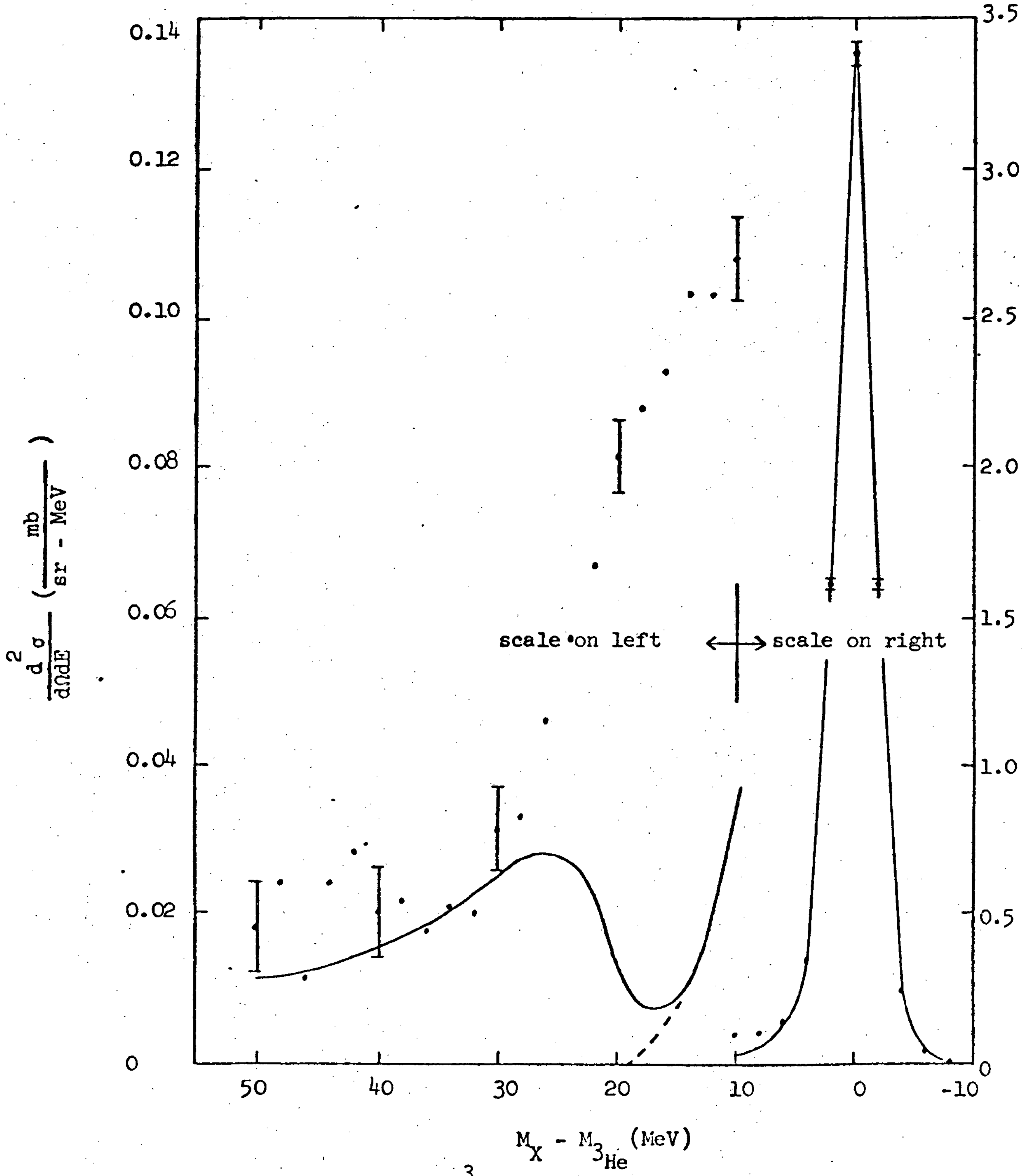

Figure 22. The energy spectrum of the ^{3}He elastic and inelastic scattering data after subtraction of the target empty data. The solid curve indicates ^{4}He elastic and inelastic scattering results and is normalized to have the same elastic scattering peak height as the ^{3}He data. The dashed curve is the extrapolation to zero of the ^{4}He elastic scattering peak. Note the scale change at 10 MeV.

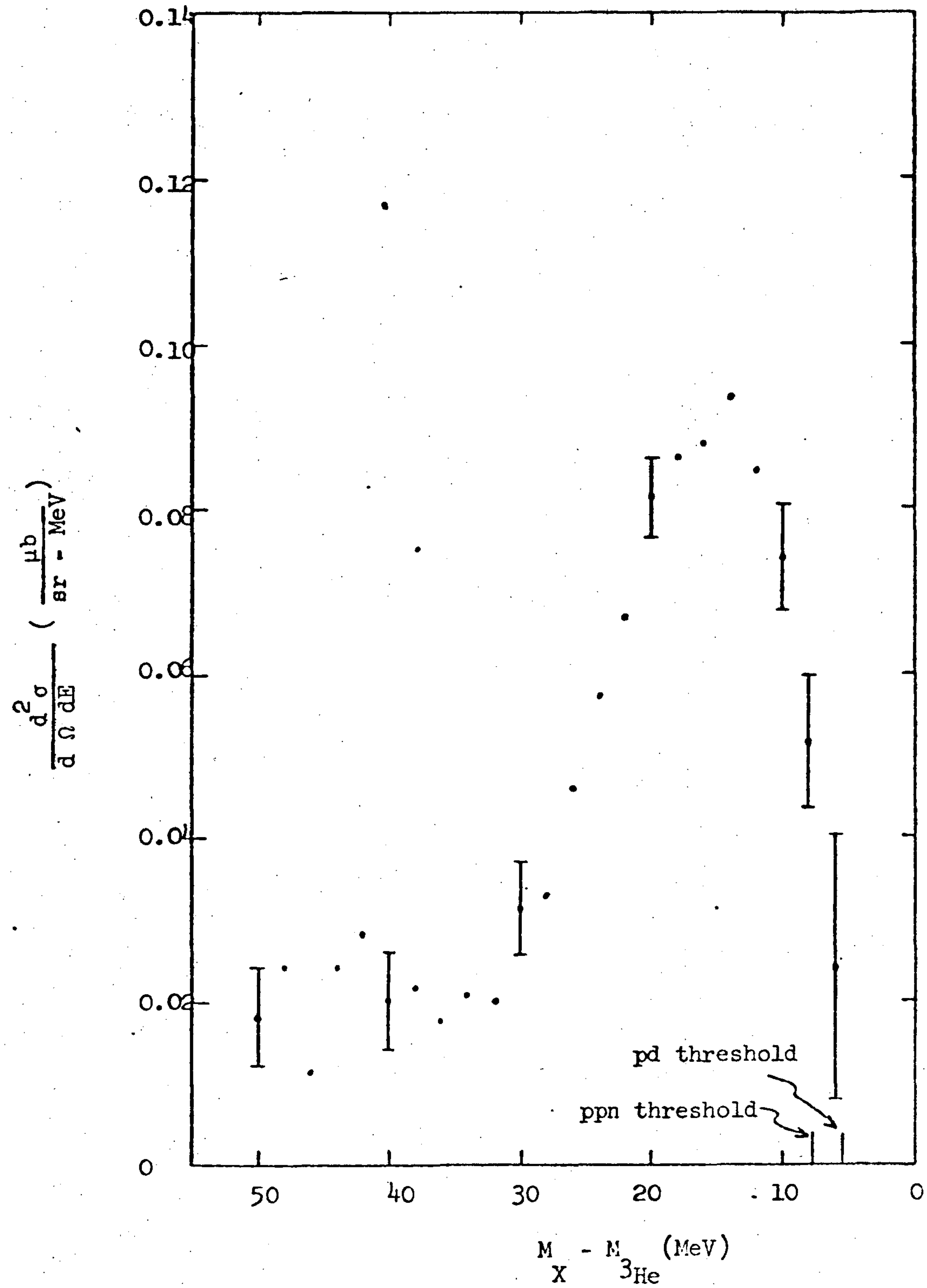

Figure 23. The energy spectrum of the ^3He inelastic scattering data. The pd and ppn thresholds are at 5.5 and 7.7 MeV respectively.

V. DISCUSSION AND CONCLUSIONS

A. Three Neutrons

In the energy region corresponding to a bound state of three neutrons there is a fairly uniform background of approximately .02 ± .007 μb/sr-MeV. Given the 6 MeV experimental energy resolution, an upper limit of .12 μb/sr is obtained for the production cross section for a bound state of three neutrons in the reaction $\pi^- + {}^3He \rightarrow \pi^+ + 3n$.

A general feature of many body final states is the fact that the spectrum of one of the emitted particles is given by the statistical model in the absence of any resonances. The solid curve in figure 19 represents the prediction of the statistical model normalized to the data in the energy range of 50 to 85 MeV for the reaction $\pi^- + {}^3He \rightarrow \pi^+ + 3n$. The dashed curve includes the effects of the ${}^1S_o$ interaction between two of the neutrons in the final state. As can be seen in the figure, neither of these curves adequately represents the measured distribution. The dot-dashed curve is the result of a calculation by Phillips.[36] He makes the assumption that double-charge-exchange occurs by a two-step process and includes the ${}^1S_o$ final state interaction. He concludes that the formation of a three-neutron system with low kinetic energy is a consequence of the three-nucleons originally being grouped together within the bound state. Calculations of the double-charge-exchange reaction have in the past been able to explain the energy distribution of the secondary pion but the predicted angular distributions have not agreed with the measured results.[23,25] Consequently a comparison of the theoretical and experimental angular distribution could be a sensitive test of Phillips' model. As can be seen in figure 20 no large angular variations are present within the limited angular range of this experiment.

It is interesting to compare our results with the results of Williams et al.[19] for the reaction ^3He (p,n)3p at 50 MeV and Kaufman et al.[15] for the reaction $\pi^- + {}^4He \rightarrow p + 3n$ at 140 MeV. Since the reactions involved different particles and were studied at different energies the magnitudes of the cross sections differ. Suppose there is T = 3/2 resonance in the three nucleon system and that the energy spectrum is determined by the three nucleon final state interaction. Then one would expect the energy spectrum in the energy region close to the resonance to be of the form

$$c|M|^2PS$$

where c is a constant determined by the particular reaction, M is the matrix element for the three-nucleon resonance, and PS is the four body phase space factor.[37] Figure 24 shows the results of the three experiments after dividing by the respective phase space factors. The normalization is adjusted to aid in the comparison. The three-proton distribution is shifted by 2 MeV as a rough correction for the coulomb effects. There is a striking similarity among the distributions which can be interpreted as evidence for the existence of an isospin 3/2

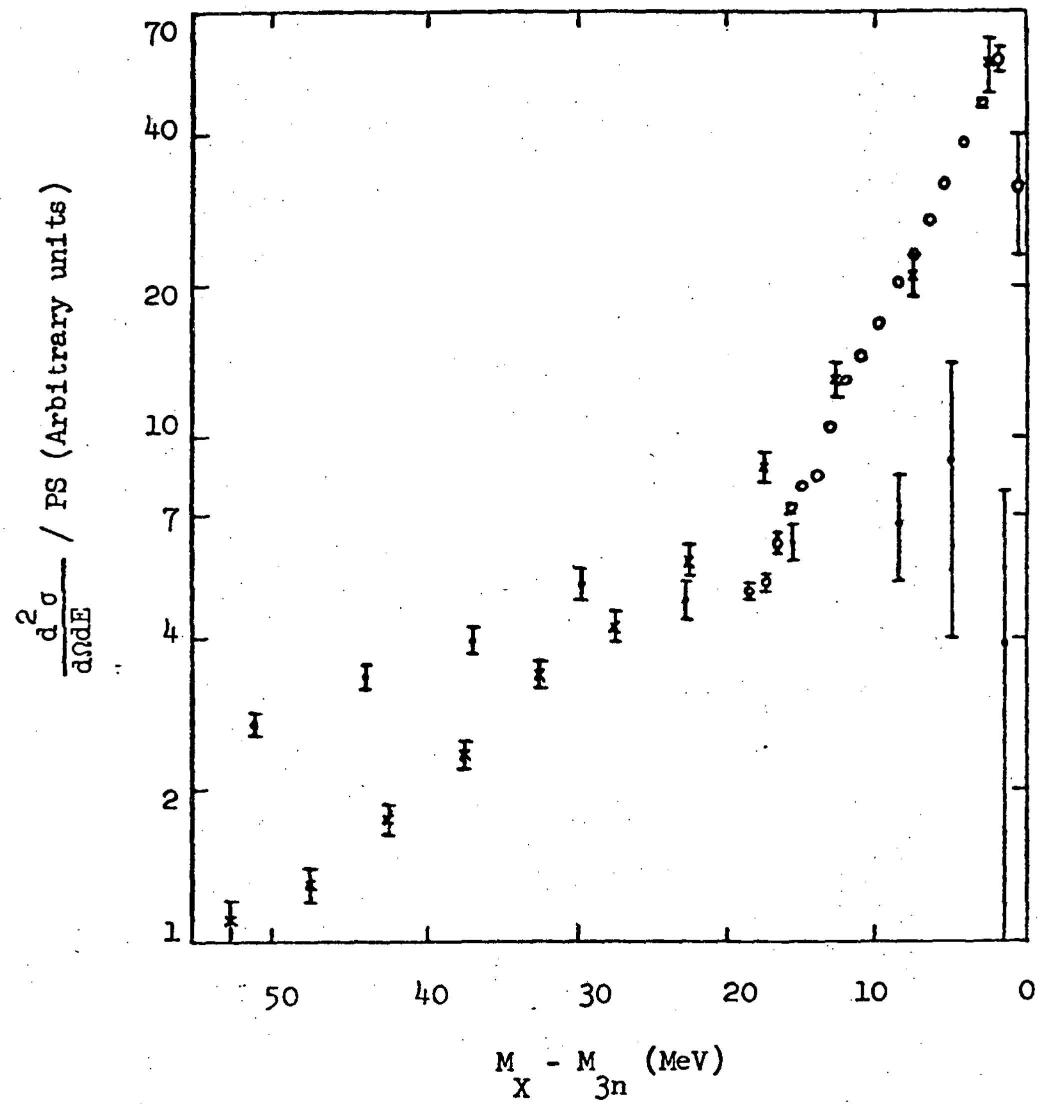

Figure 24. The energy spectrum divided by the phase space factor. The crosses are for the reaction $\pi^- + {}^3He \rightarrow \pi^+ + 3n$, the circles are for the reaction $p + {}^3He \rightarrow n + 3p$, and the dots are for the reaction $\pi^- + {}^4He \rightarrow p + 3n$. The normalizations of the spectra are adjusted to facilitate comparison.

three-nucleon resonance. Whether this interpretation of the results or the model of Phillips best explains the data awaits the existence of further experimental and theoretical study of the three-nucleon system and the double-charge-exchange reaction.

B. Inelastic Scattering

The energy resolution was insufficient to clearly separate the elastic and inelastic scattering data. However a comparison of the data from the reaction $\pi^- + {}^3He \rightarrow \pi^- + X$ with the data from the reaction $\pi^- + {}^4He \rightarrow \pi^- + X$, allows a separation of the inelastic scattering results at least in the region above 10 MeV. The resultant spectrum (figure 23) varies smoothly as a function of energy in a manner which appears to be characterized by the existence of the bound state of ${}^3He$. The effects observed in the three-neutron final state are not apparent here, probably because they are overshadowed by the proximity of the bound state.

C. Suggestions for Future Study

The main limitation of the present DCX experiment was the available pion flux. Pion beams of 100 times the intensity used in this experiment will be available at the Los Alamos Meson Physics Facility. With these intensities, angular distributions, neutron correlations, and variations with respect to the beam energy can be studied in detail. These studies can provide valuable information both on the $T = 3/2$ three nucleon system and on the DCX reaction mechanism. Based on the results of the present experiment, it would be advisable in future experiments to include a Cerenkov detector in the spectrometer to eliminate electron or positron background.

The main advantage of using pions to study the three nucleon system is that the $T = 3/2$ three-nucleon state can be reached without the complication due to additional nucleons. This advantage is compromised somewhat in inelastic scattering since the $T = 3/2$ and $T = 1/2$ contributions can not be easily separated.

ACKNOWLEDGMENTS

The successful completion of this experiment required the cooperation of many people.

I am particularly indebted to my research advisor Professor Victor Perez-Mendez for his support and guidance in this work.

The help and advice of my associates Dr. Leon Kaufman, Ben Smith, and Don Fredrickson during the preparation for and running of this experiment are greatly appreciated.

The competent and enthusiastic technical support of Don Hunt, Joe Love, and Ruth Hinkins in the running and computer analysis of the data was invaluable to the success of this project.

I would like to thank our secretary, Patricia Chatham, for cheerfully typing the many revisions of this manuscript.

Finally I greatly appreciate the patience and understanding of my wife, Sandy, and my son, Jeff, during this experiment.

APPENDICES

A. Calculation of Field Values and Integration of Orbits

The vertical component of the magnetic field B_z was measured at the midplane of the magnet ($z = 0$) and at $z = \pm 2.5$ in. on a .5 x 1.0032 in. grid. Since the field was symmetric about $z = 0$, the $z = \pm 2.5$ in. measurements were averaged and only the average values were used in the following calculations. At $z = 0$, the values of B_z, $\frac{\partial B_z}{\partial x}$, and $\frac{\partial B_z}{\partial y}$ were obtained by successive 3-point interpolations.[31] Nine points (x_i, y_j) with $i = 1,3$ and $j = 1,3$ were used in the interpolation. First, three values of $B_z(y_j)$ and $\frac{\partial B_z}{\partial x}(y_j)$ were determined using the relationships

$$B_z(y_j) = a_j x^2 + b_j x + c_j \tag{22}$$

$$\frac{\partial B_z}{\partial x}(y_j) = 2a_j x + b_j \tag{23}$$

where a_j, b_j, and c_j were determined from the known values of $B_z(x_i, y_j)$. Next $B_z(x,y)$, $\frac{\partial B_z}{\partial x}(x,y)$, and $\frac{\partial B_z}{\partial y}(x,y)$ were determined as given

$$B_z(x,y) = dy^2 + ey + f \tag{24}$$

$$\frac{\partial B_z}{\partial y}(x,y) = 2dy + e \qquad (25)$$

$$\frac{\partial B_z}{\partial x}(x,y) = py^2 + qy + r \qquad (26)$$

where d, e, f, p, q, and r were calculated using the computed values of $B_z(y_j)$ and $\frac{\partial B_z}{\partial x}(y_j)$. A similar calculation was done to obtain B_z, $\frac{\partial B_z}{\partial x}$, and $\frac{\partial B_z}{\partial y}$ at $|z| = 2.5$.

The three components of the field at an arbitrary point (x,y,z) were calculated using the interpolated values for B_z, $\frac{dB_z}{\partial x}$, and $\frac{\partial B_z}{\partial y}$ at z = 0 and z = 2.5 in. The Maxwell equation $\vec{\nabla} \cdot \vec{B} = 0$ and the boundary conditions $B_x(x,y,0) = B_y(x,y,0) = 0$ imply $\frac{\partial B_z}{\partial z}(x,y,o) = 0$. Thus the vertical component of the field was given by

$$B_z(x,y,z) = B_z(z,y,0) + [B_z(x,y,2.5) - B_z(x,y,0)](\frac{z}{2.5})^2 \qquad (27)$$

where terms of higher order in z were neglected. The Maxwell equation $\vec{\nabla} \times \vec{B} = 0$ and the boundary condition $B_x(x,y,0) = 0$ imply

$$B_x(x,y,z) = \int_0^z \frac{\partial B_x}{\partial z}(x,y,z)dz = \int_0^z \frac{\partial B_z}{\partial x}(x,y,z)\,dz$$
$$= \frac{\partial}{\partial x}\int_o^z B_z\,(x,y,z)dz$$

$$= \frac{\partial}{\partial x} \left\{ B_z(x,y,0)z + [B_z(x,y,2.5) - B_z(x,y,0)] \frac{z^3}{3(2.5)^2} \Big|_0^z \right\}$$

or

$$B_x(x,y,z) = \left\{ \frac{\partial B_z}{\partial x}(x,y,0) \right\} z + \left[\frac{\partial B_z}{\partial x}(x,y,2.5) - \frac{\partial B_z}{\partial x}(x,y,0) \right] \frac{z^3}{3(2.5)^2} \quad (28)$$

A similar expression was obtained for $B_y(x,y,z)$.

The equations for the Lorentz force $\frac{d\vec{P}}{dt} = \frac{e\,\vec{P} \times \vec{B}}{mc}$ and the relationship $\frac{d\vec{r}}{dt} = \frac{\vec{P}}{m}$ were used to integrate the particle trajectories through the magnetic field. The actual equations integrated were[38]

$$\frac{d\vec{u}}{d\tau} = \vec{u} \times \vec{B} \quad (29$$

$$\frac{d\vec{r}}{d\tau} = \vec{u} \quad (30)$$

where $\vec{u} \equiv \frac{c\vec{P}}{e}$ and $\tau \equiv \frac{et}{mc}$

A 6-vector $\vec{v}$ was defined as

$$\vec{v} \equiv \begin{pmatrix} \vec{u} \\ \vec{r} \end{pmatrix}$$

and thus

$$\frac{d\vec{v}}{d\tau} = f(\vec{v}) = \begin{pmatrix} \vec{u} \times \vec{B} \\ \vec{u} \end{pmatrix} \quad (31)$$

These equations were solved by the Adams method which gives

$$\vec{v}_{i+1} = \vec{v}_i + \frac{h}{24}[55f(\vec{v}_i) - 59f(\vec{v}_{i-1})$$

$$+ 37f(\vec{v}_{i-2}) - 9(\vec{v}_{i-3})] \tag{32}$$

when $\vec{v}_o$, $\vec{v}_1$, $\vec{v}_2$, $\vec{v}_3$ are known. The constant h is the step size and is adjusted so a decrease in the step size does not significantly increase the integration accuracy. The three additional initial conditions were calculated by a Runga-Kutta method:

$$\begin{bmatrix} \vec{k}_1 = f(\vec{v}_i) \\ \vec{k}_2 = f(\vec{v}_i + \frac{h}{2}\vec{k}_1) \\ \vec{k}_3 = f(\vec{v}_i + \frac{h}{2}\vec{k}_2) \\ \vec{k}_4 = f(\vec{v}_i + h\vec{k}_3) \\ \vec{v}_{i+1} = v_i + \frac{h}{6}(\vec{k}_1 + 2\vec{k}_2 + 2\vec{k}_3 + \vec{k}_4). \end{bmatrix} \tag{33}$$

B. Spark Chambers

1. Construction

Chambers 1 and 2 consisted of four planes of .006 in. aluminum wires (24 wires to the inch) epoxied on .375 in. Lucite and NEMA G-10 frames respectively. The central planes (the high-voltage planes) were at 90 degrees to each other and at 45 degrees to the outside (ground) planes. One of the ground planes had horizontal wires and the other had vertical wires. The purpose of having wires at other than 90 degrees to each other was to eliminate ambiguities that might otherwise arise in two-spark events. The first and last wires of each high-voltage plane were connected to the first and last wires of the corresponding ground plane with a resistor-capacitor chain (figure 25). Each time the chamber was pulsed a current flowed through the first and last wires (fiducial wires) of the planes and through the wire which carried the spark current.

The construction of chambers 3 and 4 differed from that of chambers 1 and 2 in several ways. A sheet of aluminized Mylar was placed close to each wire plane (figure 26) to improve the uniformity of the electric field in the chambers.[39] The fiducial wires were separate from the wire planes and received a separate high voltage pulse. These chambers had four planes of 0.008 in. aluminum wires spaced 24 to the inch. The two outside planes had vertical wires. The central planes had wires at 60 deg. to each other and at 30 deg. to the outside planes.

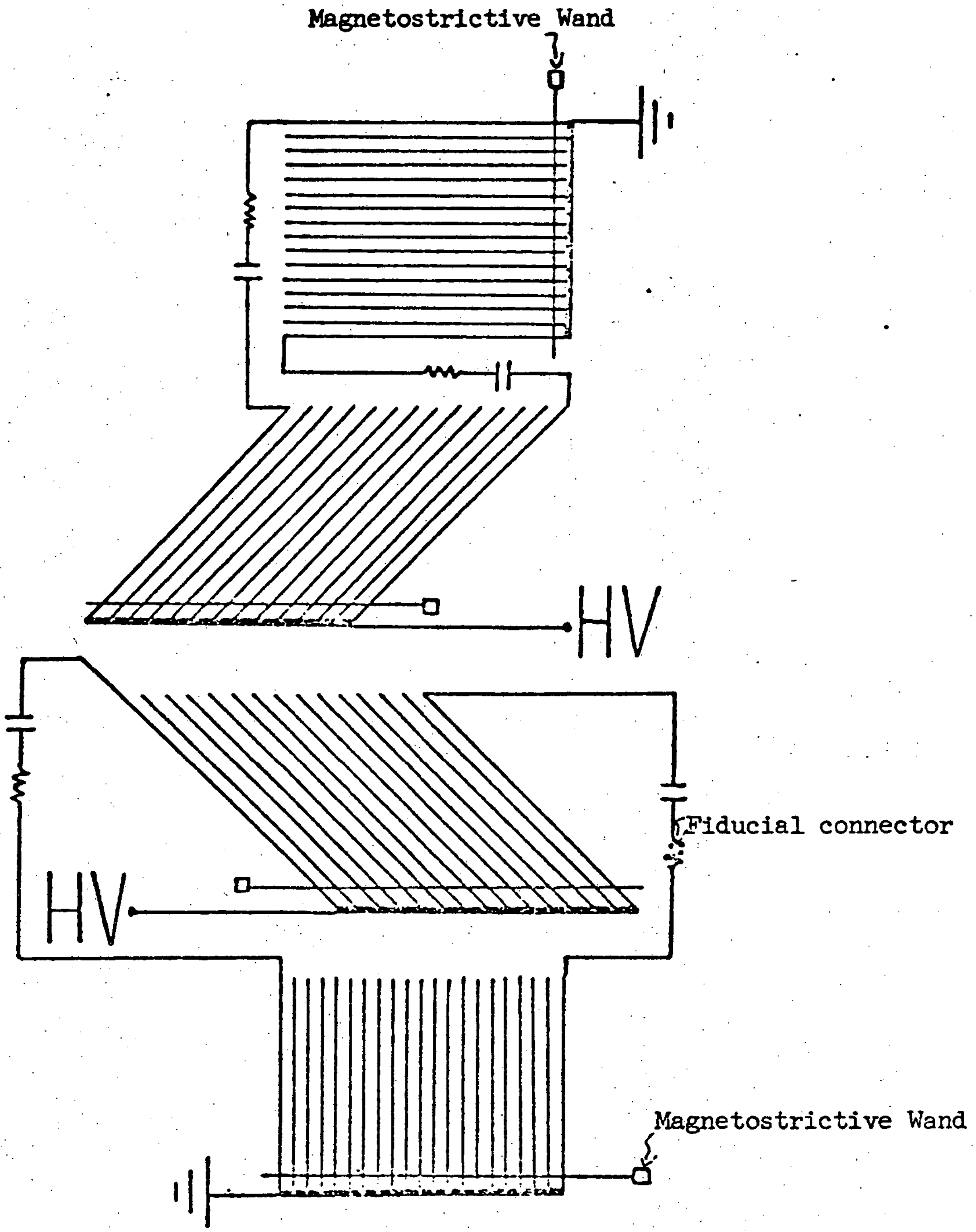

Figure 25. Schematic diagram of chambers 1 and 2 showing the fiducial wire connections and the magnetostrictive wand positions.

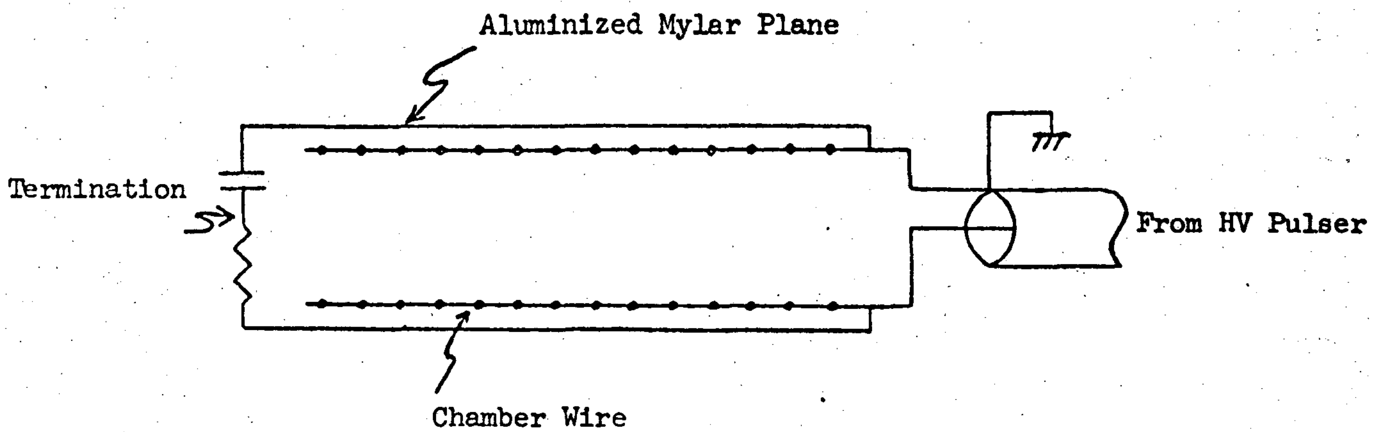

Figure 26. Schematic diagram of a single gap in chambers 3 and 4 showing the aluminized Mylar planes. Each chamber consists of two such gaps.

2. Readout

The spark positions were determined by the magnetostrictive-readout technique.[32] The basic process is as follows. A magnetostrictive line is positioned across the wires of a chamber plane (see figure 25). The magnetic field surrounding the current-carrying wire produces a local deformation in the magnetostrictive line. This deformation travels along the line with the velocity of sound (approximately 5,000 m/sec) and produces a voltage pulse in a pickup coil at the end of the line. The signal is amplified and clipped (figure 27) by an amplifier mounted on the same support that holds the magnetostrictive line. This assembly is called a wand. The signals are then differentiated and zero-crossed. The logic for digitizing the wand data is shown in figure 28. The first fiducial signal starts two scalers which count the number of pulses produced by a 20 MH_z pulser. (Note that this gives about four counts per mm. of signal propagation). The spark signal stops the first scalar and the second fiducial signal stops the second scalar. The scalar numbers are then stored on magnetic tape. The fiducial signals serve two purposes. First, their spatial location makes it possible to determine the spark location with respect to a coordinate system external to the chamber. Second, the first and second fiducial signals produce a normalizing number that is used to correct for variations in the propagation velocity of the signals due to changes in temperature, composition, density, etc.

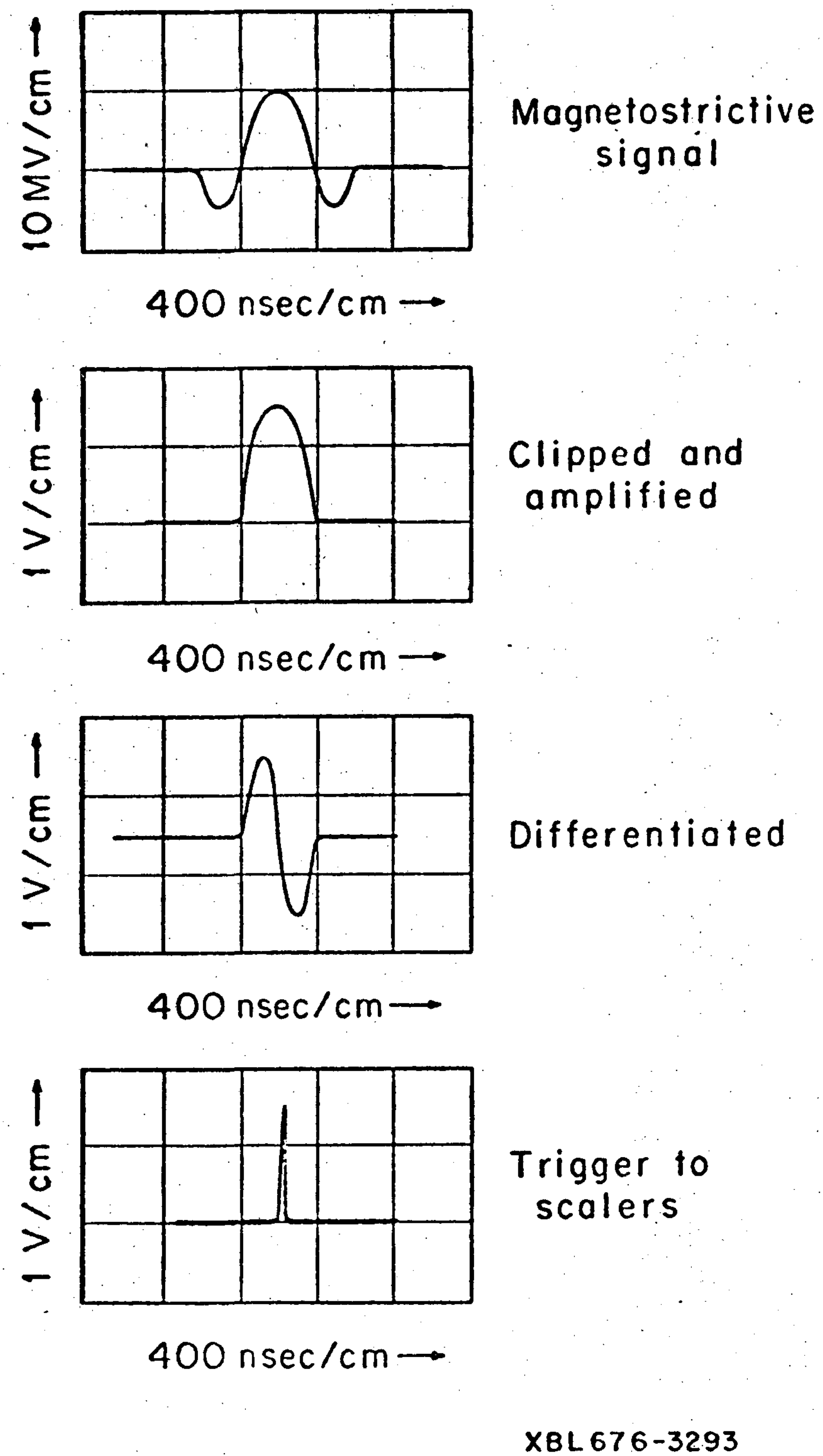

Figure 27. Pulse shapes for magnetostrictive signal processing.

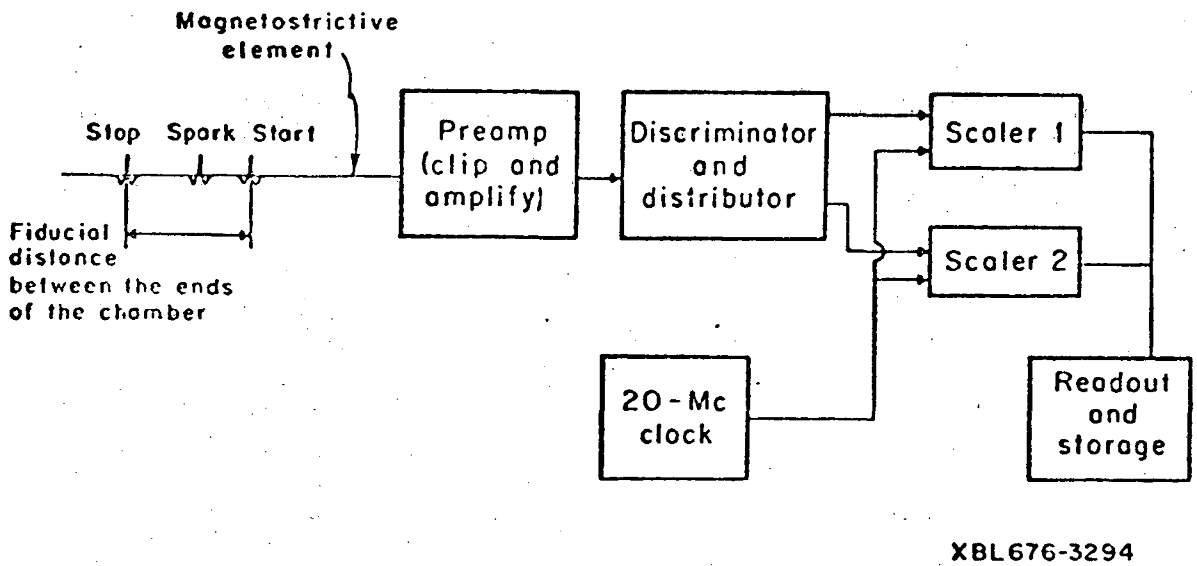

Figure 28. Simplified logic for magnetostrictive signal processing.

3. Chamber Performance

a. Efficiency: The chamber efficiency was determined from the data in Table II. The main source of inefficiency was a weak spark or a missing spark in a single gap of a chamber. The former sometimes resulted in a loss of data for one or two planes and the latter gave no signals on two wands of a chamber. As can be seen in the table this was not a serious problem. Even though two-wire fits were not used the chamber efficiencies were in all cases above 99%.

b. Accuracy: The chambers' spatial accuracy was determined from the wire-to-track deviations obtained in those cases where a track was determined by a four-wire fit in two chambers. A typical plot of the wire-to-track deviations is shown in figure 9. A spatial uncertainty of ±.02 in. is obtained from the data in the figure.

It was mentioned in section III-D that the spark location accuracy deteriorated for particles whose paths made a large angle with respect to the normal to the chamber. Figure 29 shows how the spark develops in a typical case for tracks at different angles with respect to the chamber. The 45° angle cutoff was used in the data analysis to reject events of the type shown in c.

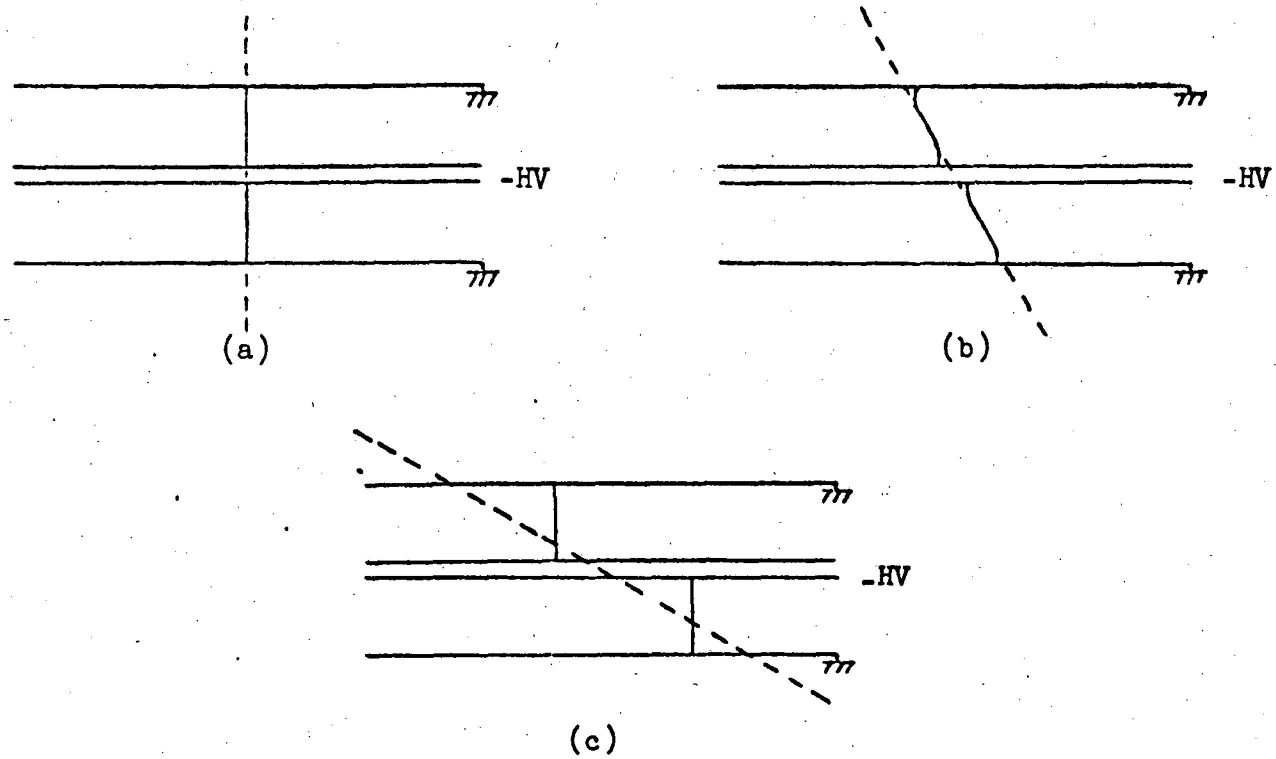

Figure 29. Sparks formed for particle path at (a) 0 deg., (b) approximately 30 deg., and (c) approximately 60 deg. The dashed lines are the particle paths and the solid curves are the sparks.

C. Spectrometer Solid Angle Acceptance

The spectrometer solid angle acceptance was determined by the Monte Carlo technique. Events were generated uniformly in the target volume, a cylinder 2-in. high and 3-in. in diameter. For a given event an interaction point (x,y, z) in the target and a direction ($\cos\theta$ and φ) were chosen. A check was performed to decide if this event satisfied the spatial limits imposed by the entrance window of the spectrometer. Assuming that this requirement was met, a momentum was chosen in the range of 60 to 260 MeV/c. The particle trajectory was integrated through the analyzing magnet and the last two spark chambers. The generated events had to satisfy requirements 3,6,7,9 and 10 of section III-D. The fraction of events F(p) as a function of the momentum p which satisfied all the above conditions and the relationship $\Omega(p) = 4\pi F(p)$ were used to find the spectrometer solid angle acceptance $\Omega(p)$. The variation of $\Omega(p)$ as a function of the momentum is shown in figure 2.

D. Positron Background

The positron background was computed by the Monte Carlo technique. The following assumptions were made:

1) The positrons were produced in the two step process

$$\pi^- + {}^3He \rightarrow \pi^o + n + n + p$$
$$\hookrightarrow \gamma + e^+ + e^- \quad .$$

2) The charge exchange reaction involved a single nucleon and the effects of the other two nucleons were neglected.

3) The π^o angular distribution was given by $3\cos^2\theta + 1$ where θ is the center of mass angle between the incoming π^- and the outgoing π^o.

4) The angular divergence of the beam was neglected.

5) The π^o decay distribution is given by[40]

$$\frac{d\sigma}{dx\,d(\cos\theta)} \propto \frac{(1-x^2)^3}{x}\left[1 + \left(\frac{2P\cos\theta''}{M}\right)^2 + \left(\frac{2Me}{M}\right)^2\right]$$

with $x = M/M_{\pi^o}$

where M_e is the electron mass, M_{π^o} is the neutral pion mass, M is the invariant mass of the electron-positron pair, P is the momentum of either the electron or the positron in the electron-positron system rest frame, and θ'' is the angle between the direction of the electron-positron system in the π^o rest frame and the direction of the positron in the electron-positron rest frame.

The event-generating procedure was as follows:

1) Choose a point in the target.

2) Choose angles θ, φ for the π^o direction. The beam direction corresponds to $\theta = 0$ and $\varphi = 0$ along the vertical direction.

3) Choose another set of angles θ', φ' to fix the direction of the electron-positron system. The axes of the primed system are parallel to the axes of the laboratory system and the origin of the primed system moves with the π^o velocity with respect to the laboratory system.

4) Choose M in the energy range of 2 Me to $M_{\pi o}$.

5) Choose a set of angles θ'', φ'' to determine the direction of the positron. Again the axes of the double-primed system are parallel to the axes of the laboratory system and the origin of the double-primed system moves with the velocity of the electron-positron system with respect to the laboratory system.

6) Using M compute the momentum of the positron and transform to the laboratory system.

7) Attempt to orbit the positron through the spectrometer.

8) Weight each successful event according to the relationship

$$W = a(1 + 3\cos^2 \theta) \cdot \left\{ \frac{(1 - x^2)^3}{x} \left[1 + \left(\frac{2P \cos \theta''}{M}\right)^2 + \left(\frac{2Me}{M}\right)^2 \right] \right\}$$

The events which were successfully orbited through the spectrometer were histogrammed as a function of their momentum. The constant "a" was adjusted so the number of events in the momentum range of 62.5-97.5 MeV/c equaled the number of experimental events (see Figure 17). With the constant "a" determined, the events were histogrammed assuming they were positive pions. The event weights were adjusted for the spectrometer solid angle acceptance and the pion decay probability. The three-neutron system mass distribution was obtained and subtracted from the experimental results (see figure 18).

Positrons can also be produced by the reaction

$$\pi^- + {}^3He \rightarrow \pi^0 + n + n + p$$
$$\quad \hookrightarrow \gamma + \gamma$$
$$\quad\quad \hookrightarrow e^+ + e^-$$

The effects of this decay mode have been similarly investigated. It was found that this type of event was only about 1/4 as frequent as Dalitz decay. The positron momentum distribution did not differ appreciably from that of Dalitz decay and therefore this process was neglected.

E. Muon Background

The muon background in the double-charge-exchange data was estimated by the Monte Carlo technique. The muons were produced by pion decay following the double-charge-exchange process

$$\pi^- + {}^3\mathrm{He} \rightarrow \pi^+ + 3n$$
$$\hookrightarrow \mu^+ + \nu_\mu$$

Since the spark positions in all four chambers were required to be consistent with a computed trajectory, these events were supposed to be rejected. The purpose of this calculation was to estimate the fraction of these events which was not rejected. The following assumptions were used in the calculation:

1) The π^+ angular distribution was isotropic in the laboratory system.

2) The μ^+ angular distribution was isotropic in the π^+ rest system.

3) The fraction of pions remaining after traveling a distance D was given $\exp(-\frac{mD}{P\tau})$

The event-generating procedure for positive pions of momentum P was as follows:

1) Choose a point (x,y,z) in the target and a direction ($\cos\theta$, φ) for the pion.

2) Choose a decay distance according to the distribution $\exp(-\frac{mD}{P\tau})$

3) Follow the particle's path for the distance D. At this point choose a direction ($\cos\theta'$, φ') for the μ^+ in the π^+ rest frame.

4) Transform the μ^+ momentum to the laboratory frame and follow the μ^+ orbit through the spectrometer. Steps 3 and 4 may not be necessary if D is large enough for the particle to travel through the spectrometer without decaying.

5) For those events which go through the spectrometer, use the four chamber intersecting points and the momentum determining routine to recompute the particle momentum. After satisfying all the criteria of section III-D approximately three percent of the remaining events were due to muons. These muons were almost all produced in pion decay between the target and the first spark chamber. The muon momentum distribution for 200 MeV/c pions is shown in figure 30. Approximately 1000 pions traveled through the spectrometer without decaying to produce the above muon background events. The structure in the distribution is due to the small number of events. The calculation was also done for pions of different momenta and the results were qualitatively the same in all cases.

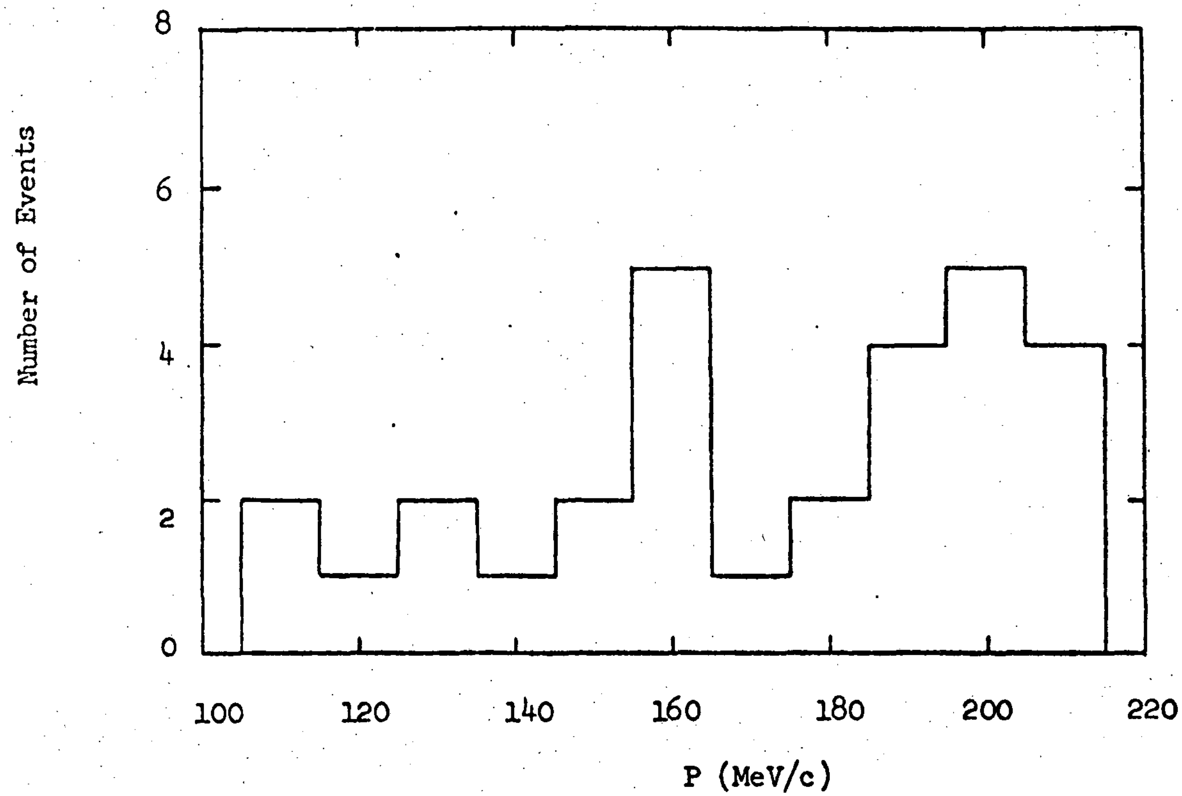

Figure 30. Momentum distribution of muons that are not rejected by the data analysis.

REFERENCES

1. A. N. Mitra and V. S. Bhasin, Phys. Rev. Letters 16, 523 (1966).
2. K. Okamoto and B. Davies, Phys. Letters 24B, 18 (1967).
3. M. Barbi, Nucl. Phys. A 99, 522 (1967).
4. H. Jacob and V. K. Gupta, Phys. Rev. 174, 1213 (1968).
5. L. M. Delves and A. C. Phillips, Rev. Mod. Phys. 41, 497 (1969).
6. R. L. Pease and H. Feshbach, Phys. Rev. 88, 945 (1952).
7. H. C. Benöhr, Nucl. Phys. A 149, 426 (1970).
8. I. R. Afnan and Y. C. Tang, Phys. Rev. 175, 1337 (1968).
9. H. Eikemeier and H. H. Hackenbroich, Z. Physik 195, 412 (1966).
10. V. Adjdačić, M. Cerineo, B. Lalović, G. Paić, I. Šlaus, and P. Tomaš, Phys. Rev. Letters 14, 444 (1965).
11. S. T. Thornton, J. K. Bair, C. M. Jones, and H. B. Willard, Phys. Rev. Letters 17, 701 (1966).
12. K. Fujikawa and H. Morinaga, Nucl. Phys. A 115, 1 (1968).
13. J. D. Anderson, C. Wong, J. W. McClure, and B. A. Pohl, Phys. Rev. Letters 15, 66 (1965).
14. J. A. Cookson, Phys. Letters 22, 612 (1966).
15. L. Kaufman, V. Perez-Mendez, and J. Sperinde, Phys. Rev. 175, 1358 (1968).
16. T. A. Tombrello and R. J. Slobodrian, Nucl. Phys. A 111, 236 (1968).
17. G. G. Ohlsen, R. H. Stokes, and P. G. Young, Phys. Rev. 176, 1163 (1968).

18. A. D. Bacher, F. G. Resmini, R. J. Slobodrian, R. DeSwiniarski, H. Meiner, and W. M. Tivol, Phys. Letters 29B, 573 (1969).

19. L. E. Williams, C. J. Batty, B. E. Bonner, C. Tschalär, H. C. Benöhr, and A. S. Clough, Phys. Rev. Letters 23, 1181 (1969).

20. R. G. Parsons, J. S. Trefil, and S. D. Drell, Phys. Rev. 138, B 847.

21. F. Becker and Z. Marić, Nuovo Cimento 36, 1395 (1965).

22. S. Barshay and G. E. Brown, Phys. Letters 16, 165 (1965).

23. Yu. A. Batusov, S. A. Bunyatov, V. M. Sidorov, and V. A. Yarba, Yad. Fix. 6, 998 (1967)[Sov. J. Nucl. Phys. 6, 727 (1968)].

24. P. E. Boynton, T. J. Devlin, J. Solomon, and V. Perez-Mendez, Phys. Rev. 174, 1083 (1968).

25. F. Becker and C. Schmit, Nucl. Phys. B 18, 607 (1970).

26. L. Gilly, M. Jean, R. Meunier, M. Spighel, J. P. Stroot, and P. Duteil, Phys. Letters 19, 335 (1965).

27. T. J. Devlin, "OPTIK," UCRL-9727 (1961)(unpublished).

28. J. Good, M. Pripstein, and H. S. Goldberg, "Cyclotron Orbits," UCRL-11044 (1963)(unpublished).

29. O. Chamberlain, Ann. Rev. Nucl. Sci. 10, 161 (1960).

30. D. Hunt, Lawrence Berkeley Laboratory, (private communication).

31. H. Weisberg and D. Snyder, "FEST", UCRL Computer Library report (unpublished).

32. V. Perez-Mendez and J. M. Pfab, Nucl. Instr. Methods 33, 141 (1965).

33. B. Rust, W. R. Burrus, C. Schneeberger, ACM 9, 381 (1966).

34. T. A. Fujii, Phys. Rev. 113, 695 (1959).

35. J. O. Kessler and L. M. Lederman, Phys. Rev. 94, 689 (1954).

36. A. C. Phillips, Phys. Letters 33B, 260 (1970).

37. K. M. Watson, Phys. Rev. 88, 1163 (1952).

38. D. C. Snyder, "ORBIT", UCRL Computer Library report (unpublished).

39. R. Grove, V. Perez-Mendez, R. Van Tuyl, Nucl. Instr. Methods 70, 306 (1969).

40. N. M. Kroll and W. Wada, Phys. Rev. 98, 1355 (1955).

TECHNICAL INFORMATION DIVISION
LAWRENCE BERKELEY LABORATORY
UNIVERSITY OF CALIFORNIA
BERKELEY, CALIFORNIA 94720